Received: 23 January 2018 | Revised: 8 May 2019 | Accepted: 6 June 2019

DOI: 10.1002/stc.2419

RESEARCH ARTICLE

WILEY

A computational framework for fast-time hybrid simulation based on partitioned time integration and state-space modeling

Giuseppe Abbiati[1] | Igor Lanese[2] | Enrico Cazzador[3] | Oreste S. Bursi[3] | Alberto Pavese[4]

[1] Institute of Structural Engineering (IBK), Department of Civil, Environmental and Geomatic Engineering (D-BAUG), ETH Zurich, Zurich, Switzerland

[2] Department of Industrial Products, EUCENTRE—European Centre for Training & Research in Earthquake Engineering, Pavia, Italy

[3] Department of Civil, Environmental and Mechanical Engineering, University of Trento, Trento, Italy

[4] Department of Civil Engineering and Architecture, University of Pavia, Pavia, Italy

Correspondence
Giuseppe Abbiati, Institute of Structural Engineering (IBK), Department of Civil, Environmental and Geomatic Engineering (D-BAUG), ETH Zurich, Stefano-Franscini-Platz 5, 8093 Zurich, Switzerland.
Email: abbiati@ibk.baug.ethz.ch

Funding information
Dipartimento della Protezione Civile, Presidenza del Consiglio dei Ministri, Grant/Award Number: RELUIS-DPC 2014-2018; Italian Ministry of Education, University and Research (MIUR), Grant/Award Numbers: 730900, L. 232/2016; Experimental Laboratory of EUCENTRE

Summary

Hybrid simulation reproduces the experimental response of large- or even full-scale structures subjected to a realistic excitation with reduced costs compared with shake table testing. A real-time control system emulates the interaction between numerical substructures, which replace subparts having well-established computational models, and physical substructures tested in the laboratory. In this context, state-space modeling, which is quite popular in the community of automatic control, offers a computationally cheaper alternative to the finite-element method for implementing nonlinear numerical substructures for fast-time hybrid simulation, that is, with testing timescale close to one. This standpoint motivated the development of a computational framework based on partitioned time integration, which is well suited for hard real-time implementations. Partitioned time integration, which relies on a dual assembly of substructures, enables coupling of state-space equations discretized with heterogeneous time step sizes. In order to avoid actuators stopping at each simulation step, the physical substructure response is integrated with the same rate of control system, whereas a larger time step size is allowed on the numerical substructure compatibly with available computational resources. Fast-time hybrid simulations of a two-pier reinforced concrete bridge tested at the EUCENTRE Experimental Laboratory of Pavia, Italy, are presented as verification example.

KEYWORDS

fast-time hybrid simulation, partitioned time integration, seismic isolation, seismic testing, state-space modeling

1 | INTRODUCTION

1.1 | Background and motivation

Hybrid simulation (HS) is a dynamic simulation paradigm that allows for investigating the experimental response of large- or even full-scale structural prototypes with reduced costs compared with shake table testing.[1-4] In detail, HS isolates the physical substructure (PS), which is experimentally tested, because it contains a key region (or component) exhibiting nonlinear behavior, from the remainder of the system, which is numerically simulated, that is, the numerical

substructure (NS). A time stepping analysis algorithm solves the coupled equations of motion of the prototype structure *online*. The term *online* indicates that calculation and measurement of NS and PS responses, respectively, are parallel tasks. In detail, at each time step of the time integration loop, displacement and velocity predictors are calculated according to the selected time stepping scheme. A set of servo-controlled actuators imposes such predictors to the PSs and measures corresponding restoring forces. Similarly, a structural analysis software provides restoring forces of NSs. Both restoring force vectors enter the coupled equation of motion of the emulated structure, which is typically solved without iterations, and the simulation moves to the next time step. In order to reduce actuator control errors, when the PS restoring force is rate independent, it is good practice to perform HS with an extended timescale $\lambda = 20 - 200$ times slower than real time, which corresponds to the so-called pseudodynamic regime, requiring inertia and damping forces of the PS to be numerically modeled. An extended simulation timescale λ reduces the destabilizing effect of actuator delay, which is typically of the order of $10 \div 20$ ms. With the term fast-time HS, we indicate a range of testing timescale $1 < \lambda < 20$, whereas real-time HS refers to the limit case of $\lambda = 1$.

Most of state-of-the-art computational frameworks for HS accommodate so-called experimental elements, which incorporate a digital interface to the control system (e.g., OpenFRESCO[5] or UI-SIMCOR[6]). The FE software, which simulates the NS, operates in soft time (e.g., on a standard PC), whereas the control system operates in hard real time and manipulates the PS by means of servo-controlled actuators. A monolithic time integration solves the coupled equation of motion. In order to coordinate HS where NS and PS responses are evaluated at different sampling rates, Pegon and Magonette[7] proposed a partitioned time integration algorithm, namely, the PM method, which coordinates two monolithic time integration processes. On the PS, an explicit time integration process runs at the sampling rate of the control system, for example, at about 1 kHz, so as to generate a continuous displacement trajectory imposed to the specimen. In order to cope with reduced computational resources, subcycling allows the time step size of the NS to be set as a multiple of the time step of the PS. Bonelli and co-workers[8] investigated the convergence and stability characteristics of the PM method, whereas Bursi and co-workers[9] proposed an enhanced variant, that is, the PM-α method, which enables the coupling of two second-order generalized-α (G-α) schemes endowed with numerical dissipation. A large experimental campaign on an existing reinforced concrete bridge was recently performed using the PM method at the Joint Research Centre (EU) of Ispra, Italy.[10]

All mentioned frameworks rely on adaptations of existing FE software and are well suited for pseudodynamic HS. It is noteworthy that the FE method allows for assembling large structural models, that is, characterized by several degrees of freedom (DoFs), by summing up mass and stiffness contributions of single elements, which are stretched over mesh nodes. A very large part of an FE code deals with calculation of element matrices, and assembly of system equations and modularity underlies the great success of the FE method. However, resulting code complexity makes FE software not suitable for hard real-time implementations required by fast-time and real-time HS.

1.2 | Scope

We deem it important to stress that prototype structures emulated via HS can be often described as lumped parameter systems characterized by a small number of DoFs. In this context, the state-space modeling approach, which is quite popular in the community of automatic control, offers a computationally cheaper alternative to FE for performing HS (e.g., Bursi et al.[11]). This standpoint motivated the development of the computational framework for HS based on state-space modeling and partitioned time integration, which is presented in this paper. As thoroughly described by means of application examples, precomputed mass and stiffness matrices of substructures plus additional differential equations can be easily used to model nonlinear structural systems endowed with hysteresis. As a result, the HS code reduces to a time stepping analysis scheme that solves the resulting set of first-order ordinary differential equations and can be easily implemented in MATLAB/SIMULINK.[12] Automatic code generation from such visual programming tools makes the process of developing hard real-time applications straightforward as shown for a two-pier reinforced concrete bridge tested at the Experimental Laboratory of EUCENTRE, Pavia, Italy, with two alternative isolation schemes.[13,14]

These are the issues that the numerical/experimental activities conducted at the EUCENTRE explore, and main findings are reported hereinafter. More precisely, the method and implementation of the partitioned time integration casted in state-space form are presented in Section 2. Section 3 discusses the verification case study, which consists of a three-bay reinforced concrete bridge provided with two alternative isolation devices. The HS experiments demonstrate the effectiveness of the proposed framework. Conclusions are drawn in Section 4.

2 | HS FRAMEWORK BASED ON PARTITIONED TIME INTEGRATION

In order to facilitate the assembly of nonlinear NSs simulated with well-known differential models, for example, Ismail et al.[15] or Mostaghel[16] hysteretic springs, the HS framework presented in this section relies on a newly conceived parallel partitioned algorithm tailored to state-space systems. More precisely, the monolithic generalized-α (MG-α) time stepping scheme proposed by Brüls and Arnold[17] is used as basic solver for the partitioned generalized-α (PG-α) method, which adopts the coupling scheme of the modified PH method conceived by Brun and co-workers.[18] Both algorithms solve the system of equations of motion recasted in state-space form that, for a generic nonlinear mechanical system, reads

$$\mathbf{M}\dot{\mathbf{Y}} + \mathbf{R}(\mathbf{Y}) = \mathbf{F}(t), \tag{1}$$

where

$$\mathbf{Y} = \begin{bmatrix} \mathbf{u} \\ \mathbf{v} \\ \mathbf{s} \end{bmatrix}, \mathbf{M} = \begin{bmatrix} \mathbf{I} & \mathbf{0} & \mathbf{0} \\ \mathbf{0} & \mathbf{m} & \mathbf{0} \\ \mathbf{0} & \mathbf{0} & \mathbf{I} \end{bmatrix}, \mathbf{R} = \begin{bmatrix} -\mathbf{v} \\ \mathbf{r}(\mathbf{u}, \mathbf{v}, \mathbf{s}) \\ \mathbf{g}(\mathbf{u}, \mathbf{v}, \mathbf{s}) \end{bmatrix}, \mathbf{F}(t) = \begin{bmatrix} \mathbf{0} \\ \mathbf{f}(t) \\ \mathbf{0} \end{bmatrix}. \tag{2}$$

In detail, $\mathbf{u}$,$\mathbf{v}$ and $\mathbf{s}$ are displacement, velocity, and additional state vectors, respectively. The former two always appear as a pair in second-order mechanical systems, whereas the latter is used to model nonlinearities endowed with memory (e.g., hysteresis). In particular, $\mathbf{r}(\mathbf{u},\mathbf{v},\mathbf{s})$ is the nonlinear restoring force vector, whereas the nonlinear function $\mathbf{g}(\mathbf{u},\mathbf{v},\mathbf{s})$ models the evolution of the additional state vector $\mathbf{s}$. Finally, $\mathbf{m}$ is the mass matrix and $\mathbf{f}(t)$ is the external time varying load, whereas $\mathbf{I}$ and $\mathbf{0}$ are identity and zero matrices, respectively. When the system is linear, velocities and displacements only characterize the system state, which does not include additional variables. As a result, (1) and (2) reduce to

$$\mathbf{M}\dot{\mathbf{Y}} + \mathbf{K}\mathbf{Y} = \mathbf{F}(t), \tag{3}$$

where

$$\mathbf{Y} = \begin{bmatrix} \mathbf{u} \\ \mathbf{v} \end{bmatrix}, \mathbf{M} = \begin{bmatrix} \mathbf{I} & \mathbf{0} \\ \mathbf{0} & \mathbf{m} \end{bmatrix}, \mathbf{K} = \begin{bmatrix} \mathbf{0} & -\mathbf{I} \\ \mathbf{k} & \mathbf{c} \end{bmatrix}, \mathbf{F}(t) = \begin{bmatrix} \mathbf{0} \\ \mathbf{f}(t) \end{bmatrix}, \tag{4}$$

with $\mathbf{k}$ and $\mathbf{c}$ stiffness and damping matrices, respectively. For simplicity, time dependency is omitted, and hereinafter, $\mathbf{M}$,$\mathbf{K}$,$\mathbf{R}$, and $\mathbf{F}$ are referred to as generalized mass, stiffness, restoring force, and external loading. First, the MG-α is analyzed; successively, the PG-α is derived through the coupling between one PS and one NS.

2.1 | The monolithic G-α time integration algorithm

2.1.1 | Description of the algorithm

The original G-α algorithm proposed by Jansen and co-workers[19] used to integrate (1) from t_n to t_{n+1} with a time integration step $\Delta t = t_{n+1} - t_n$, reads

$$\mathbf{M}\dot{\mathbf{Y}}_{n+\alpha_m} + \mathbf{R}\left(\mathbf{Y}_{n+\alpha_f}\right) = \mathbf{F}_{n+\alpha_f}, \tag{5}$$

where

$$\dot{\mathbf{Y}}_{n+\alpha_m} = (1-\alpha_m)\dot{\mathbf{Y}}_n + \alpha_m\dot{\mathbf{Y}}_{n+1}, \tag{6a}$$

$$\mathbf{Y}_{n+\alpha_f} = \left(1-\alpha_f\right)\mathbf{Y}_n + \alpha_f\mathbf{Y}_{n+1}, \tag{6b}$$

$$\mathbf{Y}_{n+1} = \mathbf{Y}_n + \dot{\mathbf{Y}}_n(1-\gamma)\Delta t + \dot{\mathbf{Y}}_{n+1}\gamma\Delta t. \tag{6c}$$

Parameters α_f,α_m,and γ define the setting of the algorithm. They are expressed as function of the infinity spectral radius ϱ_∞ parameter as

$$\alpha_m = \frac{3-\rho_\infty}{2(1+\rho_\infty)},\ \alpha_f = \frac{1}{1+\rho_\infty},\ \gamma = \frac{1}{2}+\alpha_m-\alpha_f. \tag{7}$$

In detail, if ϱ_∞ is chosen to be zero, the method annihilates the components of the system response whose frequencies are high compared with the sampling frequency. If $\varrho_\infty = 1$, then $\alpha_m = \alpha_f = \gamma = 1/2$ and the G-α method is equivalent to the trapezoidal rule, which does not introduce algorithmic dissipation. The resulting algorithm is second-order accurate.

The asynchronous balance equation of the G-α algorithm is not compatible with the dual assembly approach of the PG-α algorithm. As similarly done by Erlicher and co-workers,[20] Brüls and Arnold[17] adopted the following recurrence equation, which expresses the relationship between exact—$\dot{\mathbf{Y}}_n$, $\dot{\mathbf{Y}}_{n+1}$—and filtered—$\mathbf{V}_n$,$\mathbf{V}_{n+1}$—state derivatives:

$$(1-\alpha_m)\mathbf{V}_n + \alpha_m\mathbf{V}_{n+1} = \left(1-\alpha_f\right)\dot{\mathbf{Y}}(t_n) + \alpha_f\dot{\mathbf{Y}}(t_{n+1}) + o\left(\Delta t^2\right), \tag{8}$$

which allows for recasting (5) in a synchronous form

$$\mathbf{M}\dot{\mathbf{Y}}_{n+1} + \mathbf{R}(\mathbf{Y}_{n+1}) = \mathbf{F}_{n+1}, \tag{9}$$

with

$$\mathbf{Y}_{n+1} = \mathbf{Y}_n + \mathbf{V}_n(1-\gamma)\Delta t + \mathbf{V}_{n+1}\gamma\Delta t, \tag{10a}$$

$$\mathbf{V}_{n+1} = \dot{\mathbf{Y}}_n\left(1-\alpha_f\right)/\alpha_m - \mathbf{V}_n(1-\alpha_m)/\alpha_m + \dot{\mathbf{Y}}_{n+1}\alpha_f/\alpha_m. \tag{10b}$$

The resulting MG-α algorithm is equivalent to the Jansen's algorithm in terms of stability, accuracy, and spectral properties but is compatible with the dual assembly approach of the PG-α at the price of dealing with an extended state vector $[\mathbf{Y}_n, \mathbf{V}_n]$. With a few manipulations, it is possible to derive a predictor–single corrector form of the MG-α for integrating (1) from t_n to t_{n+1}, with a time integration step $\Delta t = t_{n+1} - t_n$, reported herein:

1. Calculation of the state predictor $\left[\widetilde{\mathbf{Y}}_{n+1}, \widetilde{\mathbf{V}}_{n+1}\right]$ at time t_{n+1},

$$\widetilde{\mathbf{Y}}_{n+1} = \mathbf{Y}_n + \dot{\mathbf{Y}}_n\gamma\Delta t\left(1-\alpha_f\right)/\alpha_m + \mathbf{V}_n\Delta t(\alpha_m-\gamma)/\alpha_m, \tag{11a}$$

$$\widetilde{\mathbf{V}}_{n+1} = \dot{\mathbf{Y}}_n\left(1-\alpha_f\right)/\alpha_m - \mathbf{V}_n(1-\alpha_m)/\alpha_m. \tag{11b}$$

2. Calculation of the state rate $\dot{\mathbf{Y}}_{n+1}$ at time t_{n+1},

$$\dot{\mathbf{Y}}_{n+1} = \mathbf{D}^{-1}\left(\mathbf{F}_{n+1} - \mathbf{R}\left(\widetilde{\mathbf{Y}}_{n+1}\right)\right), \tag{12}$$

where $\mathbf{D} = \mathbf{M} + \nabla_{\mathbf{Y}_0}\mathbf{R}\,\gamma\Delta t\alpha_f/\alpha_m$ is a matrix calculated once at the beginning of the simulation based on the generalized mass matrix $\mathbf{M}$ and the Jacobian $\nabla_{\mathbf{Y}_0}\mathbf{R}$ of the generalized restoring force vector at zero state. In this study, all Jacobians of analytical subdomains are derived via automatic differentiation by using the AdiGator Matlab toolbox.[21]

3. Calculation of the state $[\mathbf{Y}_{n+1}, \mathbf{V}_{n+1}]$ at time t_{n+1},

$$\mathbf{Y}_{n+1} = \widetilde{\mathbf{Y}}_{n+1} + \dot{\mathbf{Y}}_{n+1}\,\gamma\Delta t\alpha_f/\alpha_m, \tag{13a}$$

$$\mathbf{V}_{n+1} = \widetilde{\mathbf{V}}_{n+1} + \dot{\mathbf{Y}}_{n+1}\alpha_f/\alpha_m. \tag{13b}$$

It is noteworthy that if $\varrho_\infty = 1$, then $\alpha_m = \alpha_f = \gamma = 1/2$ and (10b) turns into

$$\mathbf{V}_{n+1} = \dot{\mathbf{Y}}_n - \mathbf{V}_n + \dot{\mathbf{Y}}_{n+1}. \tag{14}$$

If one considers $\mathbf{V}_0 = \dot{\mathbf{Y}}_0$ as initialization rule, the MG-α becomes equivalent to the trapezoidal rule. The same initialization rule is taken in this study also for the case of $\varrho_\infty < 1$, without loss of accuracy order as shown in the following section.

In order to investigate the spectral behavior of the MG-α algorithm, we introduce the following condensed notation, which recasts the procedure for integrating (3) from t_n to t_{n+1}, with a time integration step $\Delta t = t_{n+1} - t_n$ as

$$\mathbb{M}\mathbb{Y}_{n+1} + \mathbb{N}\mathbb{Y}_n = \mathbb{F}_{n+1}, \tag{15}$$

with

$$\mathbb{M} = \begin{bmatrix} \mathbf{K} & \mathbf{M} & \mathbf{0} \\ \mathbf{I} & \mathbf{0} & -\gamma\Delta t\mathbf{I} \\ \mathbf{0} & -\alpha_f\mathbf{I} & \alpha_m\mathbf{I} \end{bmatrix}, \mathbb{N} = \begin{bmatrix} \mathbf{0} & \mathbf{0} & \mathbf{0} \\ -\mathbf{I} & \mathbf{0} & -\Delta t(1-\gamma)\mathbf{I} \\ \mathbf{0} & -(1-\alpha_f)\mathbf{I} & (1-\alpha_m)\mathbf{I} \end{bmatrix}, \mathbb{Y}_n = \begin{bmatrix} \mathbf{Y}_n \\ \dot{\mathbf{Y}}_n \\ \mathbf{V}_n \end{bmatrix}, \mathbb{F}_n = \begin{bmatrix} \mathbf{F}_n \\ \mathbf{0} \\ \mathbf{0} \end{bmatrix}. \tag{16}$$

Accordingly, the time history response of (15) reads

$$\mathbb{Y}_n = \mathbb{A}^n\mathbb{Y}_0 + \sum_{i=0}^{n-1} \mathbb{A}^i\mathbb{M}^{-1}\mathbb{F}_{n-i}, \tag{17}$$

where $\mathbb{A} = -\mathbb{M}^{-1}\mathbb{N}$ is the so-called state transition matrix, which depends on both system equations and time stepping algorithm. For a generic linear second-order system described by (3) and (4), the following relation exists between modal frequency $\overline{\omega}_j$ and damping $\overline{\zeta}_j$ of the eigenmode jth after time discretization and the corresponding eigenvalue λ_j of the transition matrix $\mathbb{A}$:

$$\lambda_j = e^{-\overline{\omega}_j}\left(\overline{\zeta}_j \pm i\sqrt{1-\overline{\zeta}_j^2}\right)\Delta t \approx e^{-\overline{\omega}_j}\left(\overline{\zeta}_j \pm i\right)\Delta t, \tag{18}$$

where bars above $\overline{\omega}_j$ and $\overline{\zeta}_j$ emphasized that frequency and damping of the discretized system are inexact but eventually converge to exact values ω_j and ζ_j for Δt tending to zero. The algorithmic analysis of the MG-α method invokes all these elements, and it is presented in the following section.

2.1.2 | Algorithmic analysis

In order to analyze the algorithmic properties of the MG-α method, the following initial value problem (IVP) is taken as reference:

$$\omega^2 u + \ddot{u} = 0, \tag{19a}$$

$$u(0) = 1,\ \dot{u}(0) = 0, \tag{19b}$$

where ω is the frequency of a second-order undamped oscillator. In order to estimate the order of accuracy of the MG-α method, the solution to the IVP of (19) is discretized according to the time integration procedure described in Section 2.1.1 for different values of asymptotic spectral radius ρ_∞, and the global truncation error (GTE) is evaluated as

$$GTE = |u_n - u(t_n)| \propto \Delta t^p, \tag{20}$$

where p is the order of accuracy, u_n is the discretized solution provided by the MG-α method, and $u(t_n)$ is the analytical solution of (19), which reads

$$u(t) = \cos(\omega t). \tag{21}$$

In this respect, Figure 1 shows the GTE trend of the MG-α algorithm.

As it can be appreciated from Figure 1, the MG-α method is second-order accurate, that is, $p = 2$, with and without algorithmic damping.

In order to analyze the spectral properties of the MG-α method, the spectral radius ρ of the transition matrix $\mathbb{A}$ corresponding to the IVP of (19) was evaluated numerically for an increasing dimensionless frequency $\Omega = \omega\Delta t$. The spectral radius ρ of $\mathbb{A}$ is defined as the maximum modulus among those of all eigenvalues of $\mathbb{A}$ and is reported in Figure 2 for different values of the asymptotic spectral radius ρ_∞.

From Figure 2, one can observe that the spectral radius ρ tends to ρ_∞ as long as Ω goes to infinity. This means that algorithmic damping is provided to undamped oscillators as long as the time step size Δt is large compared with the system period $\frac{2\pi}{\omega}$. A more physical insight into the algorithmic bias is provided by dimensionless frequency $\overline{\Omega}$ and damping $\overline{\zeta}$ of the discretized system, which read

$$\overline{\Omega} = \arg(\lambda), \tag{22a}$$

$$\overline{\zeta} = -\frac{\ln(|\lambda|)}{\overline{\Omega}}, \tag{22b}$$

where λ represents the eigenvalue of the transition matrix $\mathbb{A}$ corresponding to the dimensionless frequency $\Omega = \omega\Delta t$ of the spring-mass system of (19). In this regard, Figure 3 reports plots of both discretized dimensionless frequency and damping.

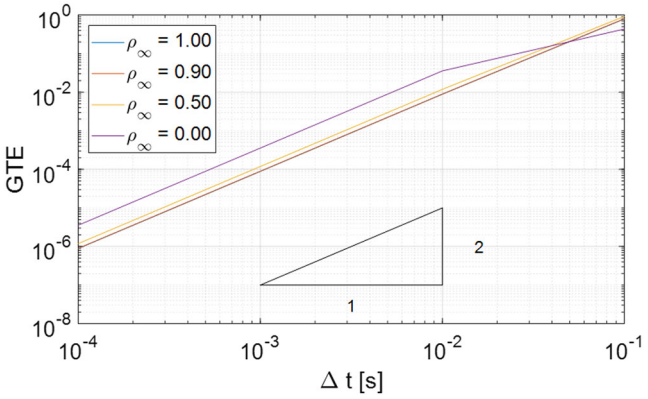

FIGURE 1 Accuracy analysis of the monolithic generalized-α method. GTE, global truncation error

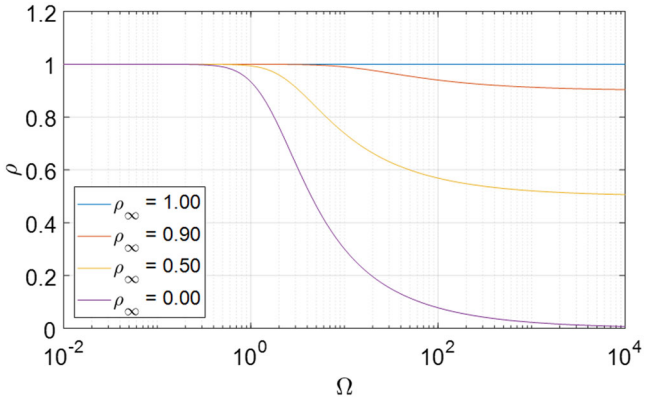

FIGURE 2 Spectral properties of the monolithic generalized-α method

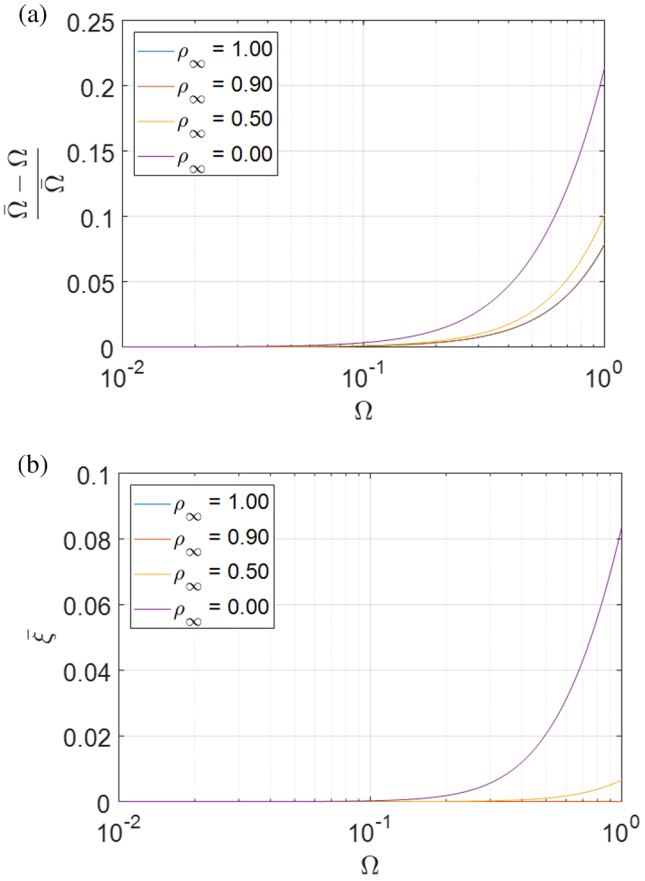

FIGURE 3 Algorithmic analysis of the monolithic generalized-α method: (a) frequency error and (b) algorithmic damping

As can be appreciated from Figure 3, lower values of ρ_∞ entail greater frequency errors $\left(\overline{\Omega}-\Omega\right)/\overline{\Omega}$ and an increasing algorithmic damping $\overline{\zeta}$.

2.2 | The partitioned G-α time integration algorithm

2.2.1 | Description of the time integration algorithm

When the so-called conventional method is used to perform HS, within a single load step, actuators approach target positions with linear ramps and, then, restoring force measurements are averaged over a time window. If load steps are large, the PS could experience load relaxation. The *continuous method* was introduced to circumvent this issue. In this case, a partitioned time integration algorithm coordinates two monolithic time integration loops running at different sampling rates. On the PS side, the time integration process runs at the control system sampling period Δt^C. Accordingly, actuators continuously move without alternating hold and ramp phases. If the control system sampling period Δt^C is too short to compute the response of the NS, the latter can be integrated with a time step multiple of Δt^C. The term *subcycling* indicates such feature. Along this line, we conceived the PG-α method, which is a partitioned time integration algorithm that couples two monolithic time integration processes based on the MG-α algorithm following a dual assembly approach. In this respect, Figure 4 depicts the task sequence of the PG-α method.

The two parallel time integration processes are coupled at the coarse time step, where the compatibility of NS and PS is forced by a dual assembly procedure. The corresponding coupled system of equations of motion reads

$$\begin{cases} \mathbf{M}^N\dot{\mathbf{Y}}^N_{n+1}+\mathbf{R}^N\left(\mathbf{Y}^N_{n+1}\right)=\mathbf{L}^N\mathbf{\Lambda}_{n+1}+\mathbf{F}^N_{n+1} \\ \mathbf{M}^P\dot{\mathbf{Y}}^P_{n+\frac{j}{ss}}+\mathbf{R}^P\left(\mathbf{Y}^P_{n+\frac{j}{ss}}\right)=\mathbf{L}^P\mathbf{\Lambda}_{n+\frac{j}{ss}}+\mathbf{F}^P_{n+\frac{j}{ss}} \end{cases}, \tag{23a}$$

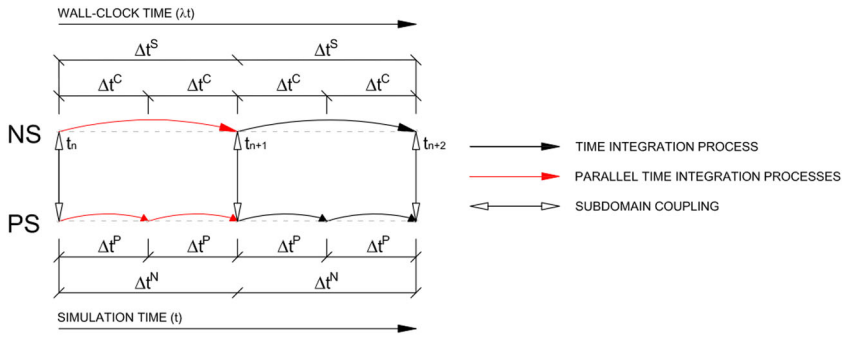

FIGURE 4 Task sequence of the partitioned generalized-α method. NS, numerical substructure; PS, physical substructure

$$\mathbf{G}^N\dot{\mathbf{Y}}^N_{n+1} + \mathbf{G}^P\dot{\mathbf{Y}}^P_{n+1} = \mathbf{0}, \tag{23b}$$

where **M**,**R**,and **F** are defined in (2), whereas signed Boolean collocation matrices **L** and **G** localize interface forces and define compatibility equations, respectively. For example, collocation matrices are reported for the benchmark case study described in the next section. In principle, at each simulation step, displacement and velocity solutions of 23 split into *free* and *link* components. The former are calculated discarding coupling conditions, which are used to compute the latter by means of a linearized Steklov–Poincaré operator. The coupled solution is the sum of both *free* and *link* contributions. According to Figure 4, two parameters define the setting of the task sequence of both the PG-α algorithm:

- the testing timescale λ, defined as $\lambda = \Delta t^C/\Delta t^P = \Delta t^S/\Delta t^N$, and
- the subcycling *ss*, obtained as $ss = \Delta t^N/\Delta t^P = \Delta t^S/\Delta t^C$.

Time steps Δt^N and Δt^P refer to simulation time, which is a virtual time axis defined by the time integration process. As an example, the seismic ground motion is expressed as a function of the simulation time. In particular, Δt^N is the coarse time step adopted for the NS, whereas Δt^P is the fine time step used to calculate the PS response. In order to guarantee a sufficient accuracy, $\Delta t^N = 1$ ms is typically considered. On the other side, Δt^S and Δt^C refer to the wall clock time, which is the real-time flow measured in the laboratory. In particular, Δt^S defines the maximum solving time that can be allocated to compute the NS response, whereas Δt^C is the actuator controller time step, which typically ranges between 1 and 2 ms. In order to guarantee smooth displacement trajectories, the PS displacement response is computed and applied to the specimen within a controller time step Δt^C. The testing timescale λ copes with actuation capacity limitations, whereas the subcycling parameter *ss* allows for adjusting Δt^S, which is the fixed time window allocated for solving the NS response. The PG-α method procedure is summarized in algorithm form for integrating 23 from t_n to t_{n+1}:

1. Initialization of the *coupled* solution,

$$\mathbf{V}_0 = \dot{\mathbf{Y}}_0 = \mathbf{M}^{-1}(\mathbf{F}_0 - \mathbf{R}(\mathbf{Y}_0)). \tag{24}$$

2. Initialization of the interface force field represented by Lagrange multipliers,

$$\mathbf{\Lambda}_0 = \mathbf{L}^{N^T}\left(\mathbf{M}^N\dot{\mathbf{Y}}^N_0 + \mathbf{R}^N\left(\mathbf{Y}^N_0\right) - \mathbf{F}^N_0\right)$$

or

$$\mathbf{\Lambda}_0 = \mathbf{L}^{P^T}\left(\mathbf{M}^P\dot{\mathbf{Y}}^P_0 + \mathbf{R}^P\left(\mathbf{Y}^P_0\right) - \mathbf{F}^P_0\right). \tag{25}$$

For the sake of simplicity, it is suggested to start the procedure considering zero initial conditions and zero initial loading so as to skip Steps 1 and 2.

3. Start the time integration loop over n from 0 to N.
4. Calculation of the *free* state predictor $\left[\widetilde{\mathbf{Y}}^{N,free}_{n+1}, \widetilde{\mathbf{V}}^{N,free}_{n+1}\right]$ at time t_{n+1},

$$\widetilde{\mathbf{Y}}_{n+1}^{N,free} = \mathbf{Y}_n^N + \dot{\mathbf{Y}}_n^N \gamma \Delta t^N (1-\alpha_f)/\alpha_m + \mathbf{V}_n^N \Delta t^N (\alpha_m - \gamma)/\alpha_m, \tag{26a}$$

$$\widetilde{\mathbf{V}}_{n+1}^{N,free} = \dot{\mathbf{Y}}_n^N (1-\alpha_f)/\alpha_m - \mathbf{V}_n^N (1-\alpha_m)/\alpha_m. \tag{26b}$$

5. Calculation of the state rate $\dot{\mathbf{Y}}_{n+1}^{N,free}$ at time t_{n+1},

$$\dot{\mathbf{Y}}_{n+1}^{N,free} = \mathbf{D}^{N^{-1}} \left(\mathbf{F}_{n+1}^{N,free} - \mathbf{R}^{\boldsymbol{N}} \left(\widetilde{\mathbf{Y}}_{n+1}^{N,free} \right) \right), \tag{27}$$

where $\mathbf{D}^N = \mathbf{M}^N + \nabla_{\mathbf{Y}_0^N} \mathbf{R}^N \, \gamma \Delta t \alpha_f / \alpha_m$ is a matrix operator calculated once at the beginning of the simulation based on the generalized mass matrix $\mathbf{M}^N$ and the Jacobian of the generalized restoring force vector $\nabla_{\mathbf{Y}_0^N} \mathbf{R}^N$, calculated at the zero state via automatic differentiation.[21]

6. Calculation of the *free* state $\left[\mathbf{Y}_{n+1}^{N,free}, \mathbf{V}_{n+1}^{N,free} \right]$ at time t_{n+1},

$$\mathbf{Y}_{n+1}^{N,free} = \widetilde{\mathbf{Y}}_{n+1}^{N,free} + \dot{\mathbf{Y}}_{n+1}^{N,free} \gamma \Delta t^N \alpha_f / \alpha_m, \tag{28a}$$

$$\mathbf{V}_{n+1}^{N,free} = \widetilde{\mathbf{V}}_{n+1}^{N,free} + \dot{\mathbf{Y}}_{n+1}^{N,free} \alpha_f / \alpha_m. \tag{28b}$$

7. Start the subcycling loop over j from 1 to ss for the calculation of the PS *free* solution.

8. Calculation of the *free* state predictor $\left[\widetilde{\mathbf{Y}}_{n+\frac{j}{ss}}^{P,free}, \widetilde{\mathbf{V}}_{n+\frac{j}{ss}}^{P,free} \right]$ at time $t_{n+\frac{j}{ss}}$,

$$\widetilde{\mathbf{Y}}_{n+\frac{j}{ss}}^{P,free} = \mathbf{Y}_{n+\frac{j-1}{ss}}^{P} + \dot{\mathbf{Y}}_{n+\frac{j-1}{ss}}^{P} \gamma \Delta t^P (1-\alpha_f)/\alpha_m + \mathbf{V}_{n+\frac{j-1}{ss}}^{P} \Delta t^P (\alpha_m - \gamma)/\alpha_m, \tag{29a}$$

$$\widetilde{\mathbf{V}}_{n+\frac{j}{ss}}^{P,free} = \dot{\mathbf{Y}}_{n+\frac{j-1}{ss}}^{P} (1-\alpha_f)/\alpha_m - \mathbf{V}_{n+\frac{j-1}{ss}}^{P} (1-\alpha_m)/\alpha_m. \tag{29b}$$

9. Calculation of the state rate $\dot{\mathbf{Y}}_{n+\frac{j}{ss}}^{P,free}$ at time $t_{n+\frac{j}{ss}}$,

$$\dot{\mathbf{Y}}_{n+\frac{j}{ss}}^{P,free} = \mathbf{D}^{P^{-1}} \left(\mathbf{F}_{n+\frac{j}{ss}}^{P,free} - \mathbf{R}^P \left(\widetilde{\mathbf{Y}}_{n+\frac{j}{ss}}^{P,free} \right) + \mathbf{L}^P \boldsymbol{\Lambda}_n \left(1 - \frac{j}{ss} \right) \right). \tag{30}$$

In line with (2) and (4), $\widetilde{\mathbf{u}}_{n+\frac{j}{ss}}^{P,free}$ and $\widetilde{\mathbf{v}}_{n+\frac{j}{ss}}^{P,free}$ are taken from $\widetilde{\mathbf{Y}}_{n+\frac{j}{ss}}^{P,free} = \left[\widetilde{\mathbf{u}}_{n+\frac{j}{ss}}^{P,free} \;\; \widetilde{\mathbf{v}}_{n+\frac{j}{ss}}^{P,free} \right]$ and imposed to the PS by means of a set of servo-controlled actuators. If an extended timescale is used, $\widetilde{\mathbf{v}}_{n+\frac{j}{ss}}^{P,free} / \lambda$ is actually imposed to the specimen. Then, the measured restoring force $\widetilde{\mathbf{r}}_{n+\frac{j}{ss}}^{P,free}$ is used to assemble the generalized physical restoring force vector $\mathbf{R}^{P^T} = \left[-\widetilde{\mathbf{v}}_{n+\frac{j}{ss}}^{P,free^T} \; \widetilde{\mathbf{r}}_{n+\frac{j}{ss}}^{P,free^T} \right]$. Similarly to Step 5, $\mathbf{D}^P = \mathbf{M}^P + \mathbf{K}^P \, \gamma \Delta t^P \alpha_f / \alpha_m$ is a constant matrix operator calculated once at the beginning of the simulation based on estimates of initial linear tangent stiffness and damping matrices of the PS. It is important to underline that additional state variables never enter the PS state vector because nonlinearities are already included in the measured restoring force.

10. Calculation of the state $\left[\mathbf{Y}_{n+\frac{j}{ss}}^{P,free}, \mathbf{V}_{n+\frac{j}{ss}}^{P,free} \right]$ at time $t_{n+\frac{j}{ss}}$,

$$\mathbf{Y}_{n+\frac{j}{ss}}^{P,free} = \widetilde{\mathbf{Y}}_{n+\frac{j}{ss}}^{P,free} + \dot{\mathbf{Y}}_{n+\frac{j}{ss}}^{P,free} \, \gamma \Delta t^P \alpha_f / \alpha_m, \tag{31a}$$

$$\mathbf{V}^{P,free}_{n+\frac{j}{ss}} = \widetilde{\mathbf{V}}^{P,free}_{n+\frac{j}{ss}} + \dot{\mathbf{Y}}^{P,free}_{n+\frac{j}{ss}} \alpha_f / \alpha_m. \tag{31b}$$

11. If $j = ss$ exit the loop, otherwise set $j = j+1$ and go to Step 8.

Before introducing Step 12, we shortly derive the Steklov–Poincaré operator, which is used to calculated *link* solutions based on *free* solutions already computed on both PS and NS. In order to do this, the PG-α method adopts the coupling strategy of the modified PH method,[18] which imposes kinematic compatibility at the end of the coarse time step Δt^N. In detail, *link* solutions are expressed as linear functions of interface Lagrange multipliers, which are obtained by linearizing decoupled subsystems equations at zero states. In order to condense the coupling procedure to a few matrix operations, the matrix notation introduced by (15) and (16) is used with the only difference that $\nabla_{\mathbf{Y}_0}\mathbf{R}$ replaces $\mathbf{K}$.

$$\begin{bmatrix} \mathbb{Y}^{P,link}_{n+\frac{1}{ss}} \\ \mathbb{Y}^{P,link}_{n+\frac{2}{ss}} \\ \vdots \\ \mathbb{Y}^{P,link}_{n+1} \end{bmatrix} = \begin{bmatrix} \mathbb{M}^P & & & \\ \mathbb{N}^P & \mathbb{M}^P & & \\ & \mathbb{N}^P & \ddots & \\ & & \ddots & \mathbb{M}^P \end{bmatrix}^{-1} \begin{bmatrix} \frac{1}{ss}\mathbb{L}^P \\ \frac{2}{ss}\mathbb{L}^P \\ \vdots \\ \mathbb{L}^P \end{bmatrix} \mathbf{\Lambda}_{n+1} = \begin{bmatrix} \mathbb{Q}^P_{\frac{1}{ss}} \\ \mathbb{Q}^P_{\frac{2}{ss}} \\ \vdots \\ \mathbb{Q}^P \end{bmatrix} \mathbf{\Lambda}_{n+1}, \tag{32a}$$

$$\mathbb{Y}^{N,link}_{n+1} = \mathbb{M}^{N^{-1}}\mathbb{L}^N\mathbf{\Lambda}_{n+1} = \mathbb{Q}^P\mathbf{\Lambda}_{n+1}, \tag{32b}$$

where $\mathbb{L}^{N^T} = \begin{bmatrix} \mathbf{L}^{N^T} & \mathbf{0} & \mathbf{0} \end{bmatrix}$ and $\mathbb{L}^{P^T} = \begin{bmatrix} \mathbf{L}^{P^T} & \mathbf{0} & \mathbf{0} \end{bmatrix}$ are signed Boolean collocation matrices that localize interface forces on state-space equations. Because our goal is to calculate the coupled solution at the coarse time step, we retain only matrix blocks $\mathbb{Q}^P$ and $\mathbb{Q}^N$ that express *link* solutions at time t_{n+1} as functions of the interface Lagrange multiplier as

$$\mathbb{Y}^{P,link}_{n+1} = \mathbb{Q}^P\mathbf{\Lambda}_{n+1}, \tag{33a}$$

$$\mathbb{Y}^{N,link}_{n+1} = \mathbb{Q}^N\mathbf{\Lambda}_{n+1}. \tag{33b}$$

If one remember that coupled solutions are sums of relevant *free* and *link* solutions,

$$\mathbb{Y}^{P}_{n+1} = \mathbb{Y}^{P,free}_{n+1} + \mathbb{Y}^{P,link}_{n+1}, \tag{34a}$$

$$\mathbb{Y}^{N}_{n+1} = \mathbb{Y}^{N,free}_{n+1} + \mathbb{Y}^{N,link}_{n+1}, \tag{34b}$$

with

$$\mathbb{Y}^{P,free}_{n+1} = \begin{bmatrix} \mathbf{Y}^{P,free}_{n+1} \\ \dot{\mathbf{Y}}^{P,free}_{n+1} \\ \mathbf{V}^{P,free}_{n+1} \end{bmatrix}, \ \mathbb{Y}^{N,free}_{n+1} = \begin{bmatrix} \mathbf{Y}^{N,free}_{n+1} \\ \dot{\mathbf{Y}}^{N,free}_{n+1} \\ \mathbf{V}^{N,free}_{n+1} \end{bmatrix}, \tag{35a}$$

$$\mathbb{Y}^{P,link}_{n+1} = \begin{bmatrix} \mathbf{Y}^{P,link}_{n+1} \\ \dot{\mathbf{Y}}^{P,link}_{n+1} \\ \mathbf{V}^{P,link}_{n+1} \end{bmatrix}, \ \mathbb{Y}^{N,link}_{n+1} = \begin{bmatrix} \mathbf{Y}^{N,link}_{n+1} \\ \dot{\mathbf{Y}}^{N,link}_{n+1} \\ \mathbf{V}^{N,link}_{n+1} \end{bmatrix}, \tag{35b}$$

where the former is calculated through Steps 4 to 10 and the latter is expressed by 33. The interface Lagrange multipliers can be easily derived from the compatibility equation (23b), which is recasted according to the expanded matrix notation,

$$\mathbb{G}^N \mathbb{Y}^N_{n+1} + \mathbb{G}^P \mathbb{Y}^P_{n+1} = \mathbf{0}, \tag{36}$$

with $\mathbb{G}^N = \begin{bmatrix} \mathbf{0} & \mathbf{G}^N & \mathbf{0} \end{bmatrix}$ and $\mathbb{G}^P = \begin{bmatrix} \mathbf{0} & \mathbf{G}^P & \mathbf{0} \end{bmatrix}$ are signed Boolean collocation matrices that localized interface DoFs on state vectors. In detail, the interface Lagrange multiplier vector relates to *free* solutions as

$$\mathbf{\Lambda}_{n+1} = -\mathbb{H}^{-1}\left(\mathbb{G}^N \mathbb{Y}^{N,free}_{n+1} + \mathbb{G}^P \mathbb{Y}^{P,free}_{n+1}\right), \tag{37}$$

where the so-called Steklov–Poincaré operator reads

$$\mathbb{H} = \mathbb{G}^N \mathbb{Q}^N + \mathbb{G}^P \mathbb{Q}^P. \tag{38}$$

At this point, we resume the description of the PG-α, which was paused at Step 11.

12. Calculation of the interface force field $\mathbf{\Lambda}_{n+1}$ according to (37).
13. Calculation of *link* solutions according to 33.
14. Calculation of *coupled* solutions according to 34.
15. If $n = N$, stop the procedure, otherwise set $n = n+1$ and go back to Step 4.

It is important to note that Steps 4 to 6, which calculate the *free* response of the NS, and Steps 7 to 11, which calculate the *free* response of the PS, are executed as parallel processes. The calculation of the *link* solution, which is performed by Steps 12 to 14, is the only process that requires exchange of information between PS and NS, which is however limited to interface kinematic quantities— $\mathbb{G}^N \mathbb{Y}^{N,free}_{n+1}$ and $\mathbb{G}^P \mathbb{Y}^{P,free}_{n+1}$—and interface forces—$\mathbf{\Lambda}_{n+1}$. In addition, because the Steklov–Poincaré matrix operator $\mathbb{H}$ is assembled and inverted once before the simulation (38), the calculation of the *link* solution consists on a simple matrix multiplication (37). These are the key points that demonstrate the superiority of partitioned algorithms with respect to monolithic time integrators for the coordination of HS.

2.2.2 | Algorithmic analysis

The benchmark case study depicted in Figure 5 was used to investigate the algorithmic properties of the PG-α method.

More precisely, the benchmark case study consists of a 2-DoF nondissipative linear system with lumped parameters and zero external loading. For the sake of example, state vectors and signed Boolean collocation matrices are also reported:

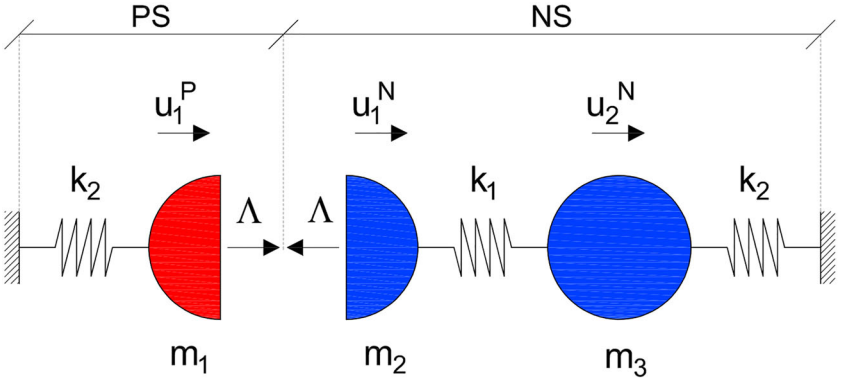

FIGURE 5 Reference split-mass two-degree-of-freedom system. NS, numerical substructure; PS, physical substructure

$$\mathbf{Y}^P = \begin{bmatrix} u_1^P \\ v_1^P \end{bmatrix}, \mathbf{L}^P = \begin{bmatrix} 0 \\ 1 \end{bmatrix}, \mathbf{G}^P = \begin{bmatrix} 1 & 0 \end{bmatrix}$$

$$\mathbf{Y}^N = \begin{bmatrix} u_1^N \\ u_2^N \\ v_1^N \\ v_2^N \end{bmatrix}, \mathbf{L}^N = \begin{bmatrix} 0 \\ 0 \\ -1 \\ 0 \end{bmatrix}, \mathbf{G}^N = \begin{bmatrix} -1 & 0 & 0 & 0 \end{bmatrix}.$$

Table 1 summarizes all parameter values for two variants of the same model; the only difference is in the m_3 values, which entails a second eigenfrequency much higher than the first for Variant 2, which is used to benchmark algorithmic dissipation.

The algorithmic analysis was performed considering the free vibration response of Variant 1 of the 2-DoFs benchmark system of Figure 5 subjected to $u_1^N = u_1^P = 0.00$ m, $u_2^N = 0.01$ m. In this respect, Figure 6 provides an overview on the order of convergence.

In detail, the trapezoidal rule algorithm was used to calculate the reference monolithic solution with a time step size of 1e − 7 s, and GTEs were evaluated at $t = 0.01$ s for several combinations of time step size, subcycling, and ρ_∞ parameters. As can be appreciated from Figure 6, the PG-α algorithm is second-order accurate regardless the values of *ss* and ρ_∞ parameters.

TABLE 1 Parameters of the benchmark system

Variant	m_1	m_2	m_3	k_1	k_2
1	4e3	4e3	9e3	4e5	5e5
2	4e3	4e3	9e0	4e5	5e5

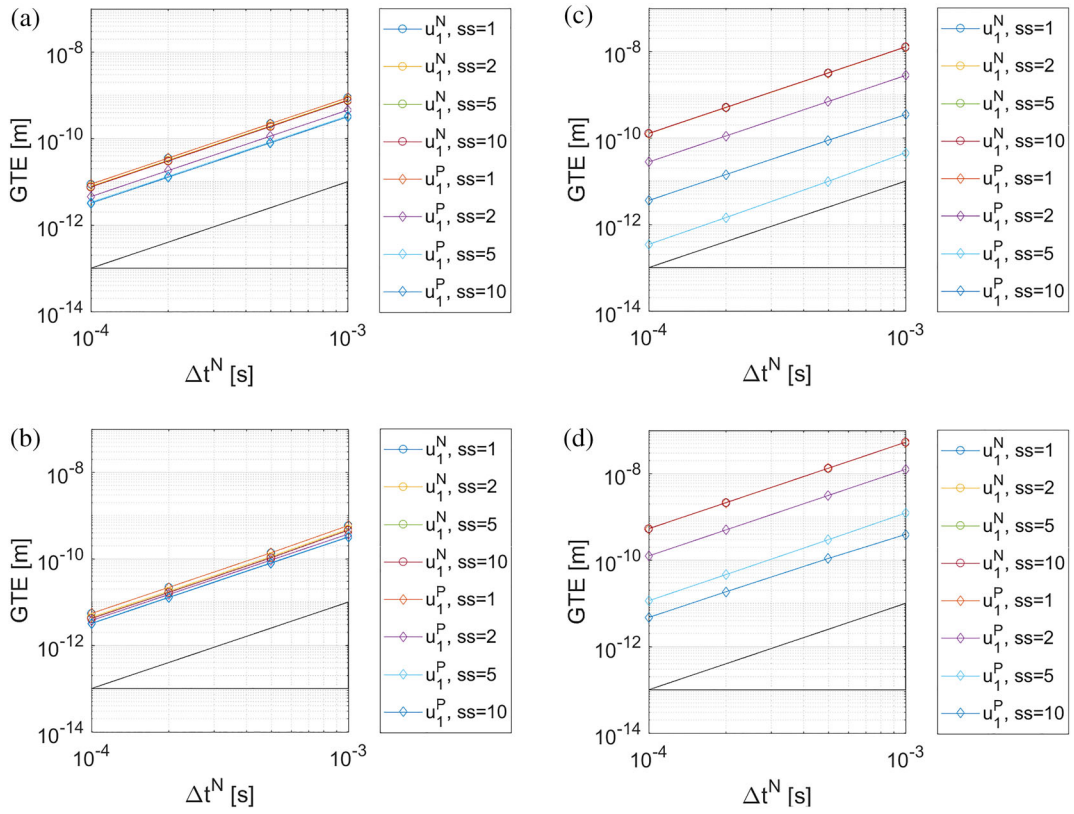

FIGURE 6 Accuracy analysis of the partitioned generalized-α method applied to Variant 1 with different *ss* and (a) $\rho_\infty = 1$, (b) $\rho_\infty = 0.9$, (c) $\rho_\infty = 0.5$, and (d) $\rho_\infty = 0.2$. The black triangle indicates the second-order accuracy slope. GTE, global truncation error

In order to investigate the algorithmic damping feature of the PG-α method, the time history response of Variant 2 was calculated with the same initial conditions and zero external loading of the former analysis for a time span of 2 s and considering different values of ρ_∞. A careful reader may notice that Variant 2 is characterized by a very small mass on the right node. This has been intentionally done in order to emphasize the algorithmic damping properties of the PG-α method on stiff systems. In this regard, both Figures 7 and 8 compare the displacement response of the system obtained with different values of ρ_∞ parameter.

One can observe that the maximum response peak is preserved when $\rho_\infty = 1$. On the other hand, the more ρ_∞ tends to zero, the faster the high-frequency component of the response associated with the small value of m_3 is damped out.

Another important feature of the PG-α method, which is inherited from the coupling scheme of the modified PH method, is that the algorithm is energy preserving when $\rho_\infty = 1$. This has been verified numerically by computing the instantaneous total energy (i.e., kinematic plus potential elastic) of Variant 2 for the same IVP. In this respect, Figure 9 summarizes the results. Clearly, the algorithmic is energy preserving both with and without subcycling.

3 | EXPERIMENTAL VERIFICATION OF THE HS FRAMEWORK

In order to verify the proposed computational framework, we conceived a two-pier bridge virtual prototype used to benchmark alternative seismic isolation schemes at the Experimental Laboratory of EUCENTRE, Pavia, Italy.[22]

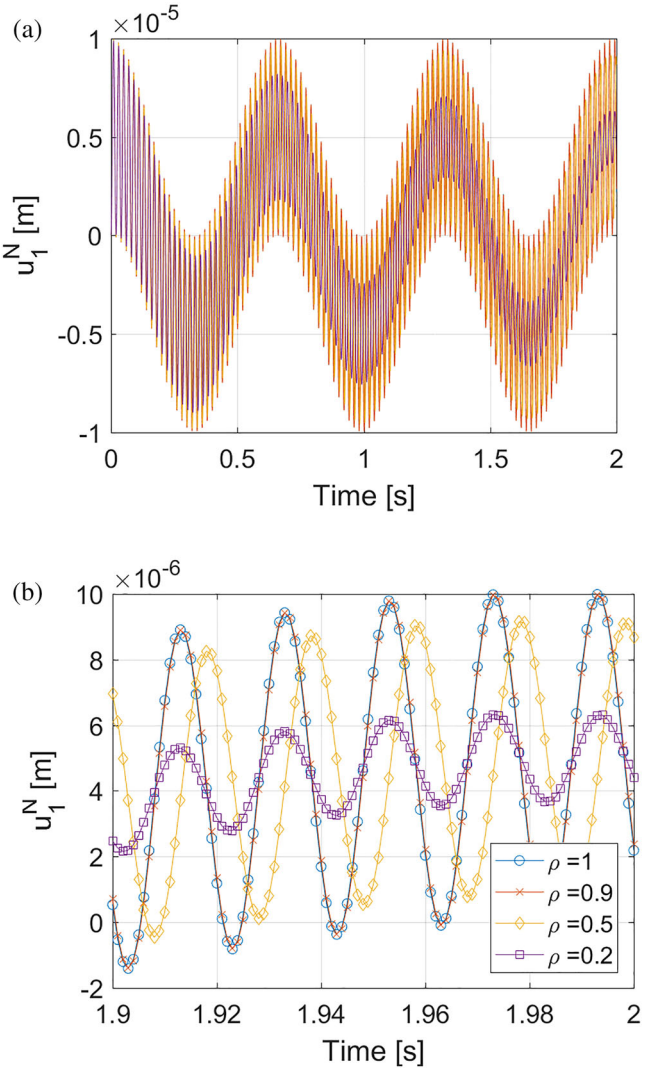

FIGURE 7 Time history response of u_1^N of Variant 2 with $ss = 1$, $\Delta t^N = 1e-3$ s: (a) full simulation span and (b) zoom on the final portion of the displacement time histories

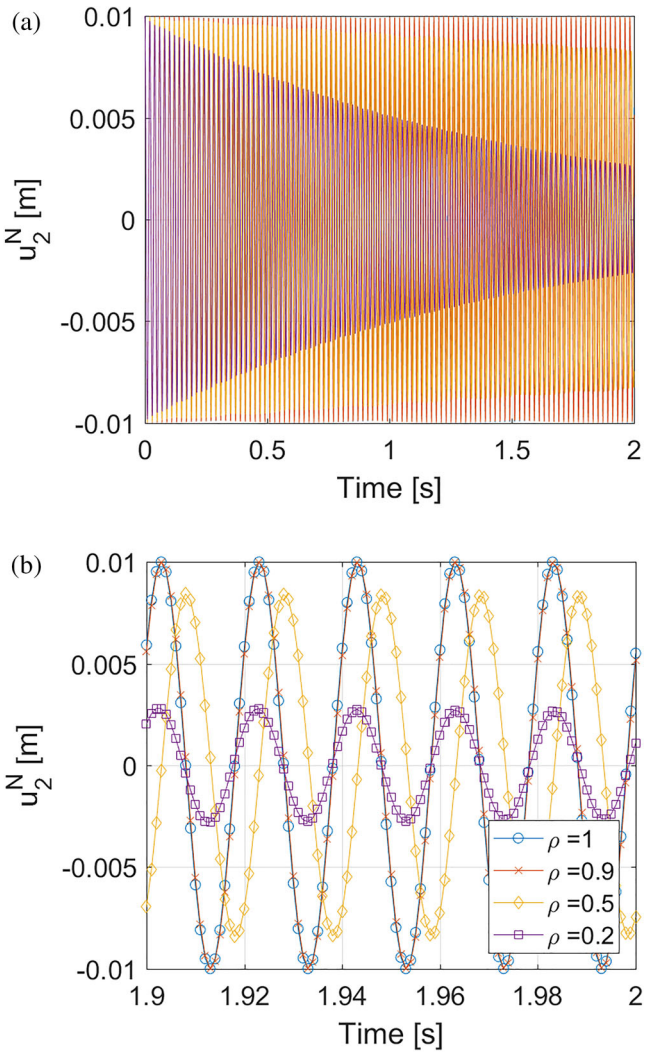

FIGURE 8 Time history response of u_2^N of Variant 2 with $ss = 1$, $\Delta t^N = 1e-3$ s: (a) full simulation span and (b) zoom on the final portion of the displacement time histories

3.1 | The virtual bridge prototype

The virtual reinforced concrete bridge prototype was characterized by a three-span deck with two independent roadways, sustained by two twin cantilever rectangular hollow cross-section piers. Figure 10 depicts a schematic of the bridge prototype.

Cross sections of deck and pier are depicted in Figure 11, whereas Table 2 summarizes relevant geometrical properties.

As depicted in Figure 10, a pair of seismic isolation devices is interposed between the deck and each pier, and two additional seismic isolator pairs are interposed between deck and abutments. In this study, we considered two alternative seismic isolation schemes based on lead rubber bearings (LRBs) and triple curvature concave sliding bearings (T-CSBs), both designed to preserve piers from damage in the case of a seismic event. All devices were selected to keep the maximum transversal shear force applied to each pier below 370 kN and the corresponding transversal displacement below 10 mm. In this respect, Figure 12 reports the schematics of both types of seismic isolation devices including pictures taken from the test setup.

A more detailed description of each tested isolation device including related computational models is reported in Section 3.2.

In order to support the design of the HS campaign, a reference FE model of the bridge without isolation devices was implemented in OpenSEES.[23] Linear beam elements were used for the deck, whereas fiber-based nonlinear beam

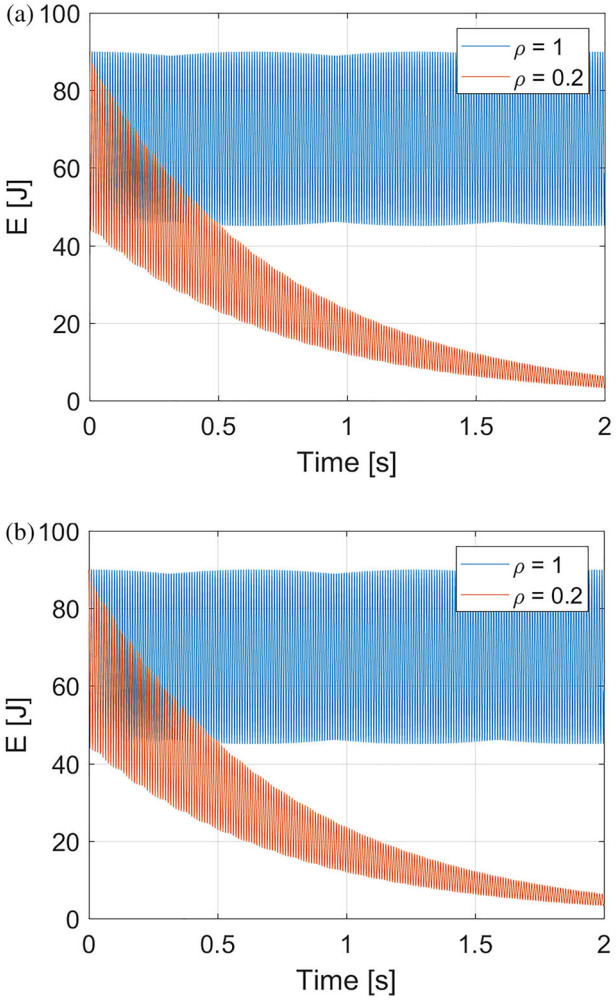

FIGURE 9 Instantaneous total energy of Variant 2: (a) $ss = 1$ and (b) $ss = 10$

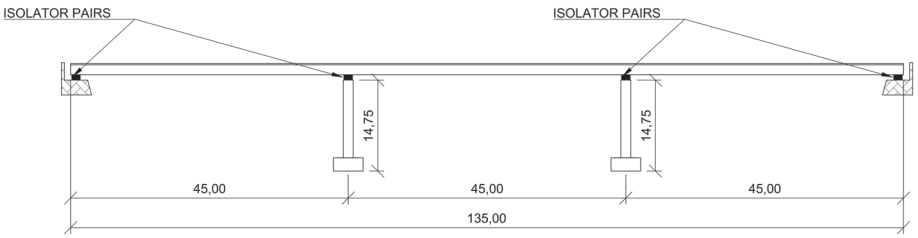

FIGURE 10 Virtual bridge prototype

elements were used for piers, thus reproducing positions and dimensions of rebars. Figure 13 depicts a schematic of the OpenSEES FE model with node numbering and constraint conditions.

Rigid links accounted for the offset between pier cap beams and deck center of gravity, as depicted in Figure 14. In addition, y and z relative rotations between deck and rigid links were released.

Values of material parameters were calibrated based on results of previous quasistatic cyclic tests performed on a 1:2 scale mock-up specimen of the pier.[24] A proportional Rayleigh damping model was used considering an equivalent viscous damping of 5% on Modes 1 and 5, which were characterized by the two highest modal participation factors with respect to the direction of the seismic loading. Table 3 reports the first five vibration periods of the bridge in the as-built configuration predicted by the OpenSEES FE model.

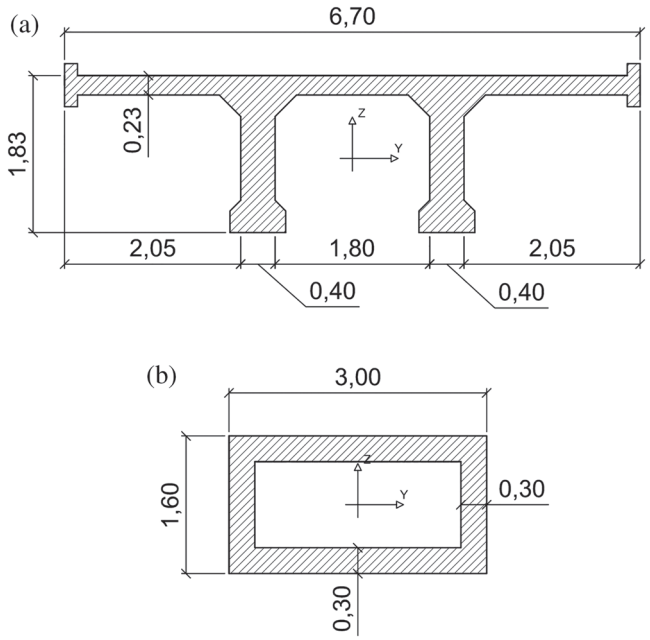

FIGURE 11 Cross sections of (a) deck and (b) pier

TABLE 2 Geometrical properties of cross sections

Property	Deck	Pier
A	2.78 m^2	2.40 m^2
I_{zz}	7.20 m^4	0.82 m^4
I_{yy}	0.85 m^4	2.40 m^4

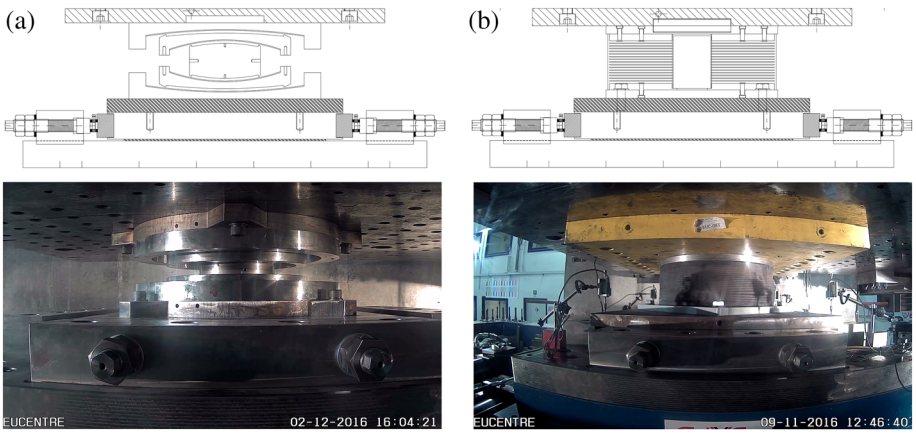

FIGURE 12 Tested seismic isolation devices: (a) triple curvature concave sliding bearing and (b) lead rubber bearings

The REXEL software[25] was used to select a single ground motion record corresponding to a seismic scenario characterized by moment magnitude $M = 5 \div 7$, epicentral distance $D = 0 \div 30$ km, and soil type B. Target values of peak ground acceleration (PGA) for scaling the accelerogram were identified by means of time history response analyses of the OpenSEES FE model. In detail, a PGA = 0.12 g was assigned to the serviceability limit state (i.e., onset of a nonlinear response of piers), whereas a PGA value of 0.30 g was selected for the ultimate limit state (i.e., highly nonlinear response of piers). In this regard, Figure 15 depicts both the accelerogram and the relevant elastic acceleration response spectrum for the ultimate limit state case highlighting the bridge periods reported in Table 3.

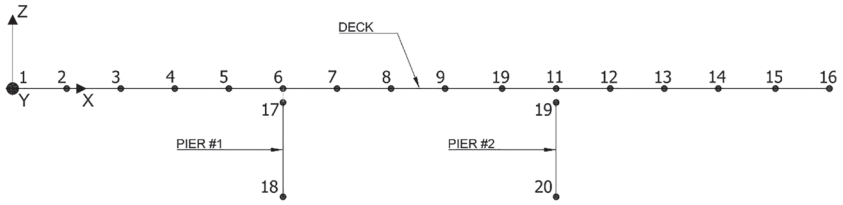

FIGURE 13 OpenSEES FE model of the virtual prototype bridge

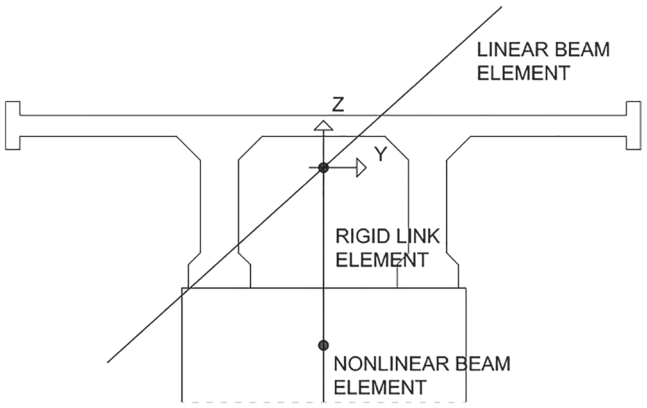

FIGURE 14 Deck-pier connection based on rigid link elements

TABLE 3 Vibration periods of the virtual prototype bridge in the configuration AB

Mode	Period (s)
1	0.639
2	0.500
3	0.392
4	0.344
5	0.320

3.2 | Substructuring of the bridge

In order to compare the structural performance of two isolation schemes based on T-CSB and LBR, respectively, a single isolation device was substructured in the laboratory as PS, whereas the remaining substructures of the virtual bridge prototype were numerically simulated. In this regard, Figure 16 reports a schematic of the substructuring scheme adopted for HS.

The schematic reported in Figure 16 must be intended as a plan view of the bridge. Nonlinear springs represent isolation devices, which are activated by the in-plane transversal motion of the deck. The linear springs represent the two twin piers, which experience an elastic response. Piers and deck mass and stiffness matrices were obtained via static condensation. In particular, the deck superelement was obtained by retaining transversal displacements of Nodes 1, 6, 11, and 16 of the OpenSEES FE model; see Figure 13 in this respect.

3.2.1 | Triple-surface concave sliding bearings

The selected T-CSB was designed by EUCENTRE. Figure 17 depicts a schematic of a generic T-CSB device, for which a detailed mechanical model can be found in Fenz and Constantinou.[26]

Table 4 summarizes the main dimensions of the T-CSB device, whereas Table 5 provides values of μ for different velocity peak values.

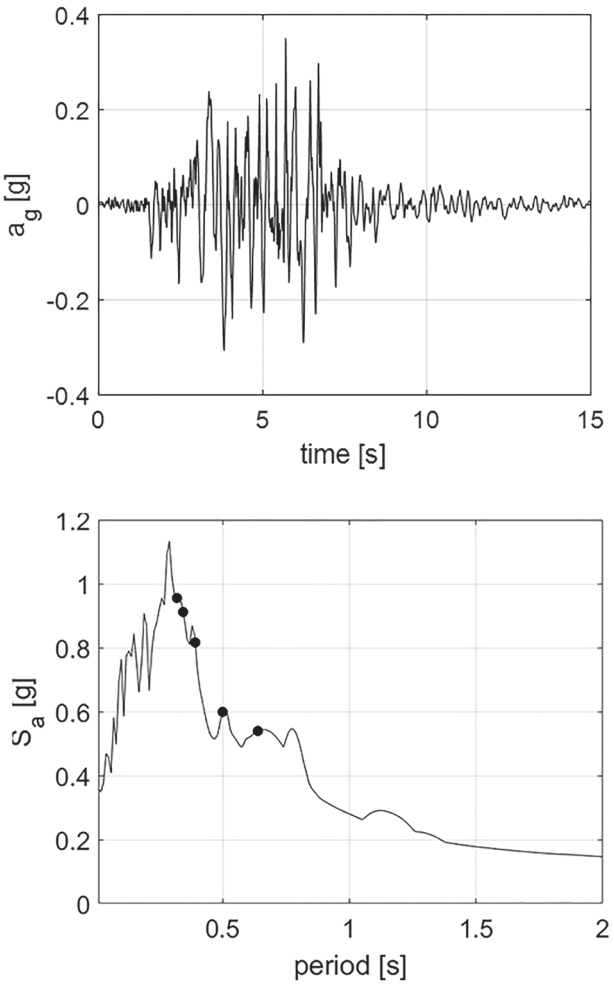

FIGURE 15 Selected seismic ground motion scaled to peak ground acceleration = 0.30 *g* for the ultimate limit state: (a) accelerogram and (b) acceleration response spectrum for an equivalent viscous damping of 5.00% (dots indicate the first five periods of the bridge without isolation devices)

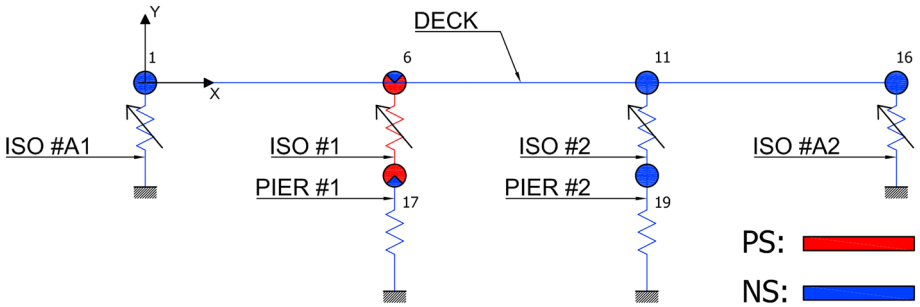

FIGURE 16 Substructuring of the virtual bridge prototype. NS, numerical substructure; PS, physical substructure

For a nominal vertical load $P = 1{,}500$ kN, contact pressures of 15.6 and 47.7 MPa characterize internal and external surfaces, respectively. In order to reproduce the hysteretic response of the T-CSB on the NS, a state-space model was assembled based on the nonlinear spring proposed by Mostaghel.[16] In this regard, Figure 18 shows both the spring-slider idealization and the resulting hysteresis loop.

The state-space model of the restoring force r is described as

$$\dot{r} = \dot{r}_0 + \dot{r}_1 + \dot{r}_2, \tag{39a}$$

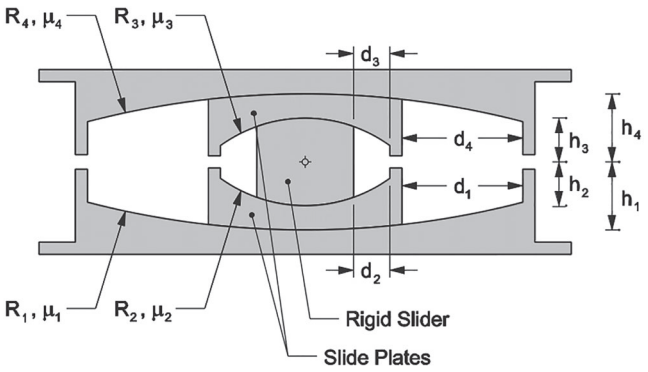

FIGURE 17 Schematic of a triple curvature concave sliding bearing device after Fenz and Constantinou[26]

TABLE 4 Main dimensions of triple curvature concave sliding bearing (T-CSB)

External surfaces (1–4)	Internal surfaces (2–3)
$R_1 = R_4 = 1{,}600$ mm	$R_2 = R_3 = 500$ mm
$h_1 = h_4 = 90$ mm	$h_2 = h_3 = 60$ mm
$d_1 = d_4 = 38$ mm	$d_2 = d_3 = 53$ mm

TABLE 5 Identified values of friction coefficients

Velocity (mm/s)	0.5	5	25	50	100
$\mu_{1,4}$ (%)	8.5	12.0	14.0	14.0	15.0
$\mu_{2,3}$ (%)	4.5	6.0	7.0	7.0	7.5

$$\dot{r}_0 = \left(k_0\left(\overline{N}(v)\overline{M}(s_0 - \delta_0) + M(v)N(s_0 + \delta_0)\right)\right)v, \tag{39b}$$

$$\dot{r}_1 = \left(k_1\left(\overline{N}(v)\overline{M}(s_1 - \delta_1) + M(v)N(s_1 + \delta_1)\right)\right)v, \tag{39c}$$

$$\dot{r}_2 = k_2 v, \tag{39d}$$

where slip displacements of equivalent sliders read

$$s_1 = r_1/k_1, \tag{40a}$$

$$s_2 = r_2/k_2, \tag{40b}$$

and functions N, M, $\overline{N}$, and $\overline{M}$ are defined as follows:

$$\begin{aligned} N(w) &= 0.5(1 + \operatorname{sgn}(w))(1 + (1 - \operatorname{sgn}(w))) \\ M(w) &= 1 - N(w) \\ \overline{N}(w) &= M(-w) \\ \overline{M}(w) &= N(-w). \end{aligned} \tag{41}$$

Values of model parameters identified for the maximum velocity peak of 0.1 m/s read

$$k_0 = 6.67\text{e}7\ \text{N/m},\ \delta_0 = 1.5\text{e} - 3\ \text{m},\ k_1 = 1.15\text{e}6\ \text{N/m},\ \delta_1 = 0.07\ \text{m},\ k_2 = 5\text{e}5\ \text{N/m}.$$

The developed model was validated against experimental data. In this respect, Figure 19 compares emulated and measured hysteretic loops and dissipated energy histories. As can be appreciated, the developed model accurately reproduces the response of the tested T-CSB device.

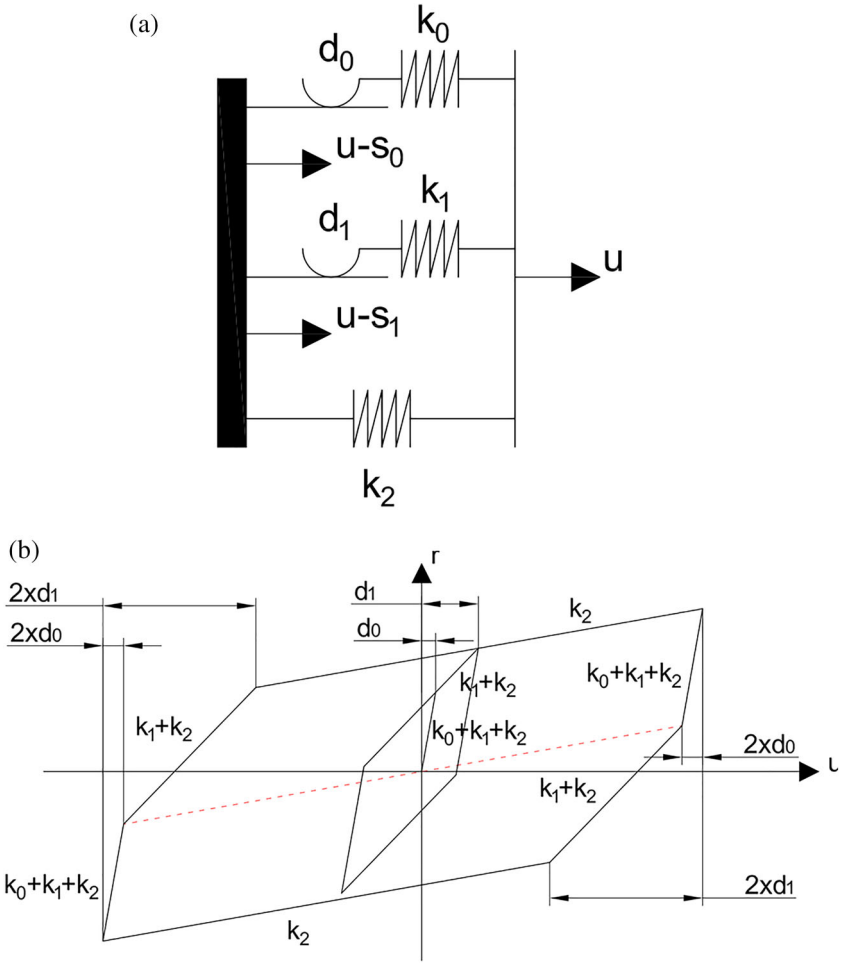

FIGURE 18 Triple curvature concave sliding bearing state-space model: (a) spring-slider idealization and (b) hysteretic loop

3.2.2 | Lead rubber bearings

A third seismic isolation scheme based on LRB isolation devices was also tested at EUCENTRE. In order to emulate LRBs on the NS, the model developed by Benzoni and co-workers[27] was adopted. In this respect, Figure 20 shows a schematic view of a generic LRB with main components highlighted, whereas Figure 21 depicts idealized hysteretic loops.

The governing equations of the LRB restoring force model read

$$r = r_1 + r_2, \tag{42a}$$

$$r_1 = \frac{k_{\text{rubber}}}{2}\left(u + p\cdot \text{sgn}(u)\left|\frac{u}{p}\right|^{n_{\text{rubber}}}\right), \tag{42b}$$

$$r_2 = \text{sgn}(v) r_{\text{lead}}\left(1 - 2\exp\left(-a_{\text{lead}}\left(1 + \text{sgn}(v)\frac{u}{p}\right)\right) + 4\left(1 + \text{sng}(v)\frac{u}{p}\right)\exp\left(-(a_{\text{lead}} + \ln(2))\left(1 + \text{sgn}(v)\frac{u}{p}\right)\right)\right). \tag{42c}$$

The parameter n_{rubber} determines the postyielding nonlinear behavior of rubber, whose degradation is governed by the additional state variable p, which tracks the absolute displacement peak of the device,

$$\begin{cases} \dot{p} = v\cdot \text{sgn}(u),\ |u| \geq p \\ \dot{p} = 0,\ |u| < p \end{cases}. \tag{43}$$

In addition, the parameter a_{lead} governs the smoothing of the loading/unloading branches of the hysteretic loop generated by yielding of lead core. A remarkable advantage of the adopted model is that all parameters, except n_{rubber} and

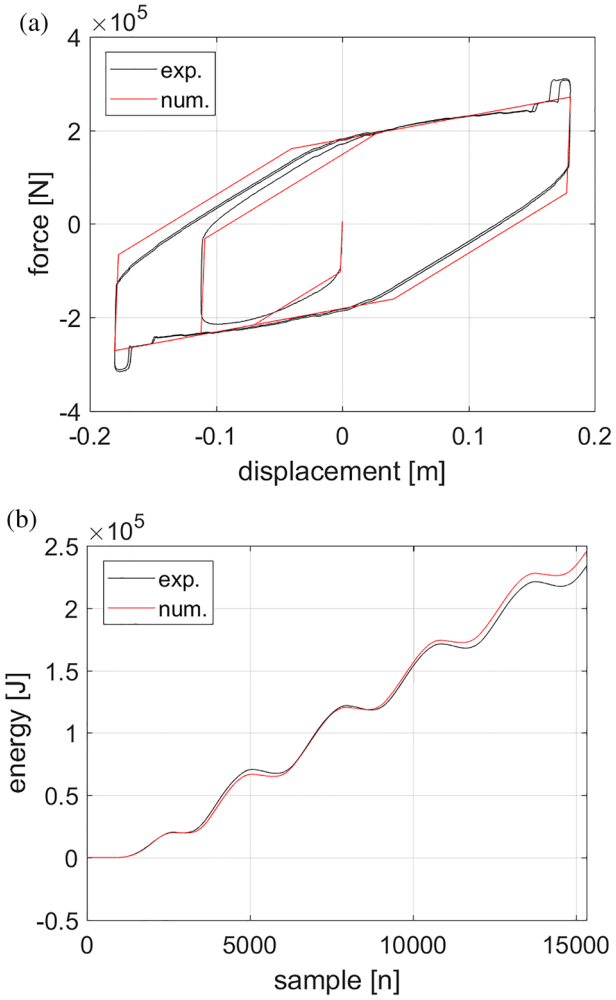

FIGURE 19 Validation of the triple curvature concave sliding bearing model against experimental measurements at $v = 0.1$ m/s: (a) hysteretic loop and (b) dissipated energy

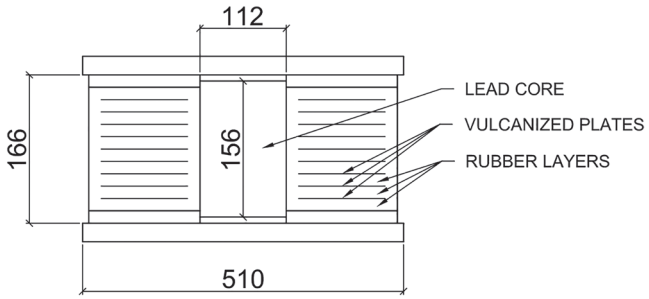

FIGURE 20 Schematic of the lead rubber bearing with main dimensions in millimeters

a_{lead}, can be derived from geometric and material properties of the LRB device,

$$r_{\text{lead}} = A_{\text{lead}}\tau_{\text{lead}} = 1.02\text{e}5\ \text{N}, \tag{44a}$$

$$k_{\text{rubber}} = \frac{A_{\text{rubber}}G_{\text{rubber}}}{h_{\text{rubber}}} = 1.35\text{e}6\ \text{N/m}, \tag{44b}$$

where A_{rubber} and h_{rubber} are base area and thickness of the rubber cylinder, whereas G_{rubber} is the shear elastic modulus of the rubber material. Similarly, A_{lead} is the cross-section area of the lead core, whereas τ_{lead} defines the yielding shear

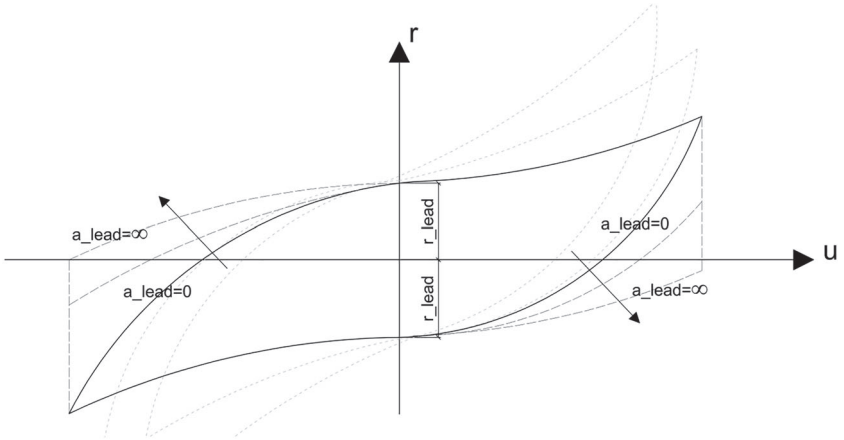

FIGURE 21 Hysteretic loop of the lead rubber bearing model after Benzoni and Casarotti [27]

stress of lead. All these parameters are taken from the LRB datasheet, whereas $n_{\text{rubber}} = 2$ and $a_{\text{lead}} = 5$ are found through the minimization of the restoring force error with respect to measured data from LRB characterization tests. As a result, Figure 22 compares the response of the calibrated LRB model to measured data. The calibrated model accurately reproduces the response of the actual LRB device at large displacement amplitudes but does not capture pinching phenomena at small displacements. However, the developed model is deemed sufficiently accurate for representing LRB devices on the NS.

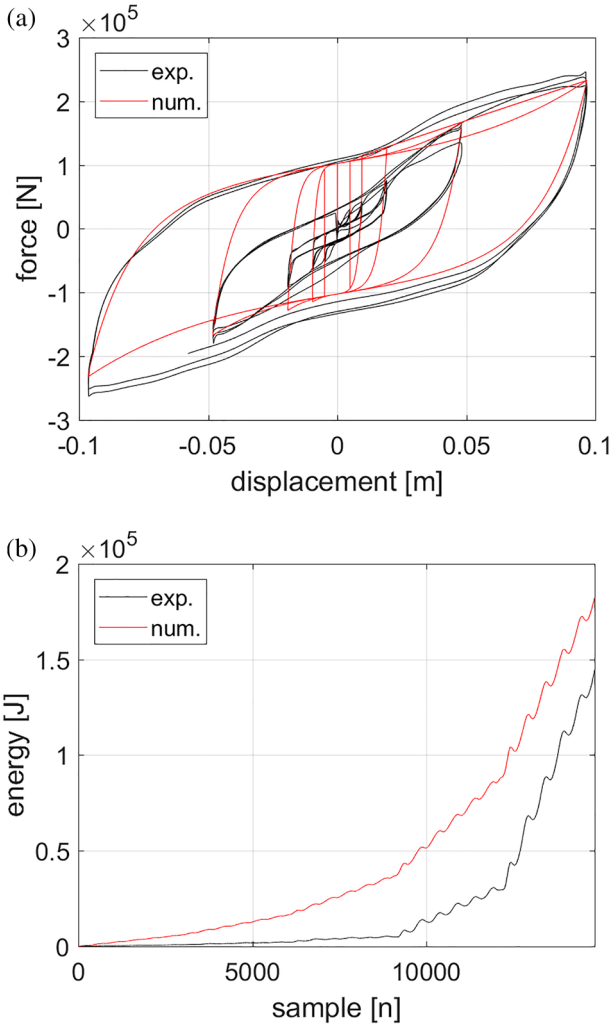

FIGURE 22 Validation of the lead rubber bearing model against experimental measurements: (a) hysteretic loop and (b) dissipated energy

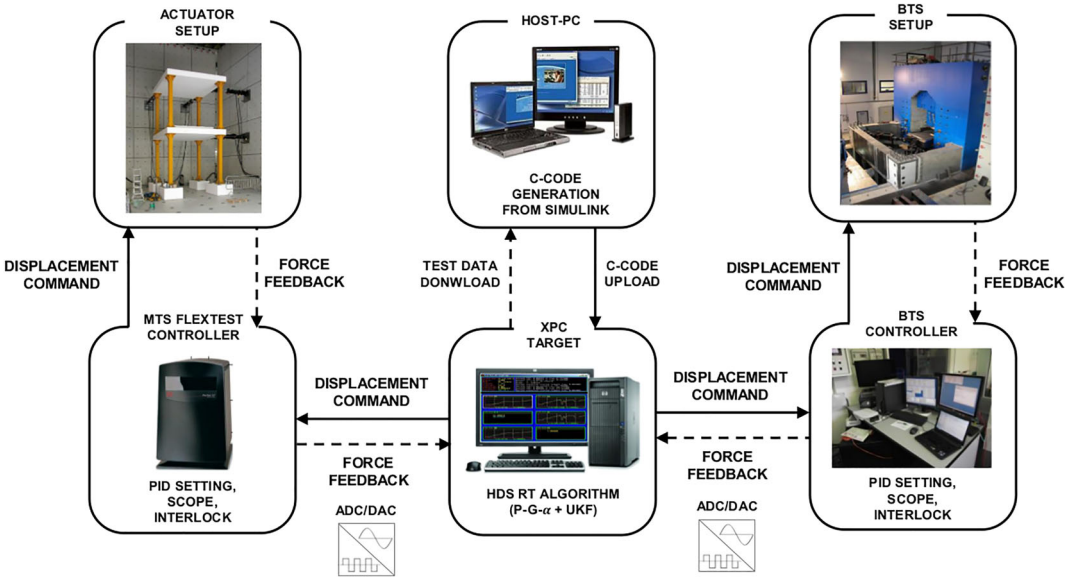

FIGURE 23 Block diagram of the hybrid simulation framework. BTS, bearing testing system

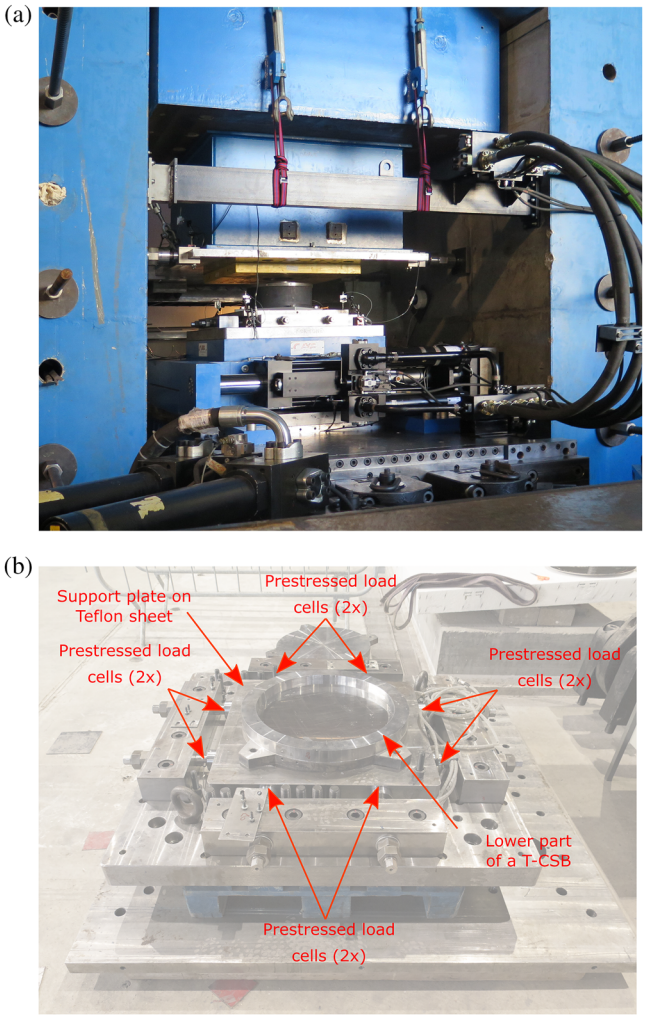

FIGURE 24 Bearing testing system: (a) test setup with a lead rubber bearing device installed and (b) force measuring system based on prestressed load cells

3.3 | Laboratory implementation at EUCENTRE

In order to simulate the virtual bridge prototype, the HS framework of Figure 23, which relies on the PG-α algorithm described in Section 2.2, was implemented at the Experimental Laboratory of EUCENTRE, Pavia, Italy. A Windows-based HOST-PC runs the MATLAB–SIMULINK computational environment,[12] which implements both the PG-α algorithm and the NS of the substructured system. The C-code automatically generated by SIMULINK is compiled and uploaded to the XPC-TARGET that executes the software in hard real time. The XPC-TARGET is provided with DAQ boards that communicate with both the MTS FLEXTEST controller, which is used to control servo-hydraulic

TABLE 6 Program of the HT5 testing campaign

Test	Date	Configuration	Timescale λ	PGA (g)	PS
HT5-14	11/11/2016	ISO 2	16	0.30	LRB
HT5-16	11/11/2016	ISO 2	16	0.50	LRB
HT5-38	01/12/2016	ISO 2	16	0.30	T-CSB
HT5-40	01/12/2016	ISO 2	16	0.50	T-CSB

Abbreviations: LRB, lead rubber bearing; PGA, peak ground acceleration; PS, physical substructure; T-CSB, triple curvature concave sliding bearing.

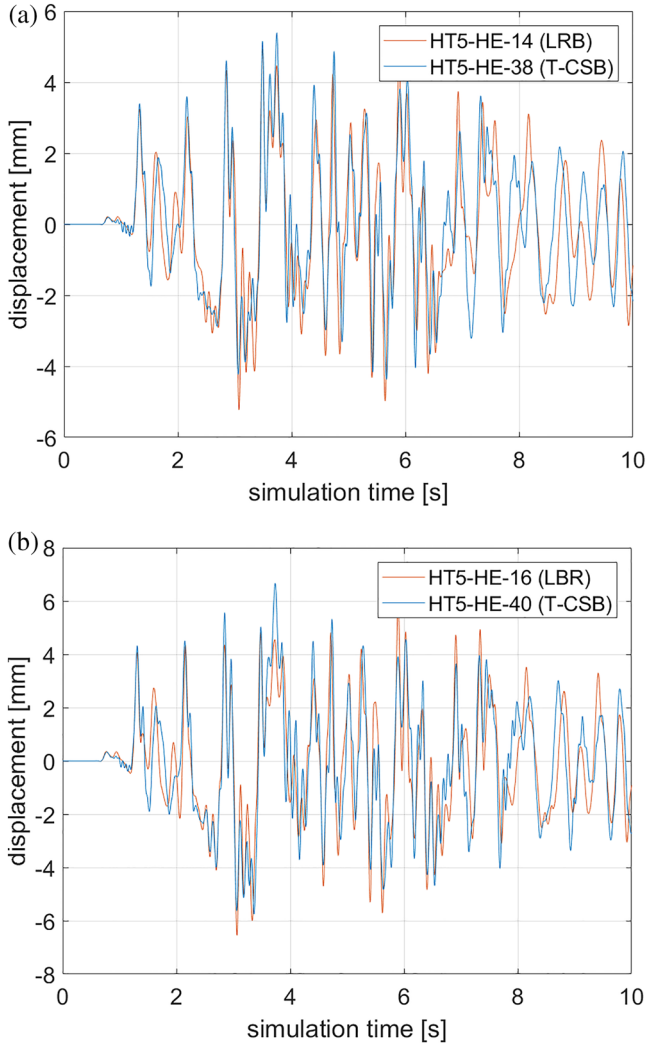

FIGURE 25 Simulated displacement response histories of Pier 2: (a) peak ground acceleration = 0.35 *g* and (b) peak ground acceleration = 0.50 *g*. LRB, lead rubber bearing; T-CSB, triple curvature concave sliding bearing

actuators, and the bearing testing system (BTS) controller, which controls a servo-hydraulic loading system specifically conceived for testing bearings. At each simulation step of the PG-α algorithm, the XPC-TARGET sends displacement commands to both MTS FLEXTEST and BTS controllers, and restoring forces measured by both actuation systems are fed back to the PG-α algorithm that solves the system of coupled equations of motion. In order to enable fast-time HS, the delay compensation algorithm proposed by Wu and co-workers[28] was adopted.

The BTS of the Experimental Laboratory of EUCENTRE was designed to impose realistic boundary conditions to full-scale seismic isolation devices.[22] In detail, the specimen is positioned on a self-equilibrating vertical reaction structure; the bottom plate of the specimen is connected to a 6-DoF shake table, driven by vertical and horizontal actuators and connected to an additional horizontal reaction structure, which can be operated in mixed force–displacement control. The maximum vertical and horizontal load capacities of the BTS are 50 and 2.8 MN, respectively. The allowed horizontal displacement range is ±495 mm with a velocity peak of 2,200 mm/s. In order to eliminate spurious friction and inertia components, eight ring prestressed load cells measure both components of the horizontal restoring force of the tested isolation device directly from its support plate, which slides on a Teflon sheet. In this regard, Figure 24 shows the BTS setup and provides a close-up view of the restoring force measuring system.

It is worthy to note that the interaction between displacement controlled actuators and stiff specimens easily triggers dynamic instability. This situation is very likely to occur on elements subjected to axial deformation, where small displacement perturbations generate large feedback forces. In order to overcome this problem, the common practice consists on excluding vertical DoFs from the HS loop and to impose nominal loads in force control. Accordingly, the nominal vertical load owing to the self-weight of the bridge deck was kept constant and applied to the tested seismic isolation device in force control. In addition, a single bearing per pair was physically tested, and the measured restoring force fed back to the HS algorithm was doubled. This latter simplification was preliminary verified with numerical

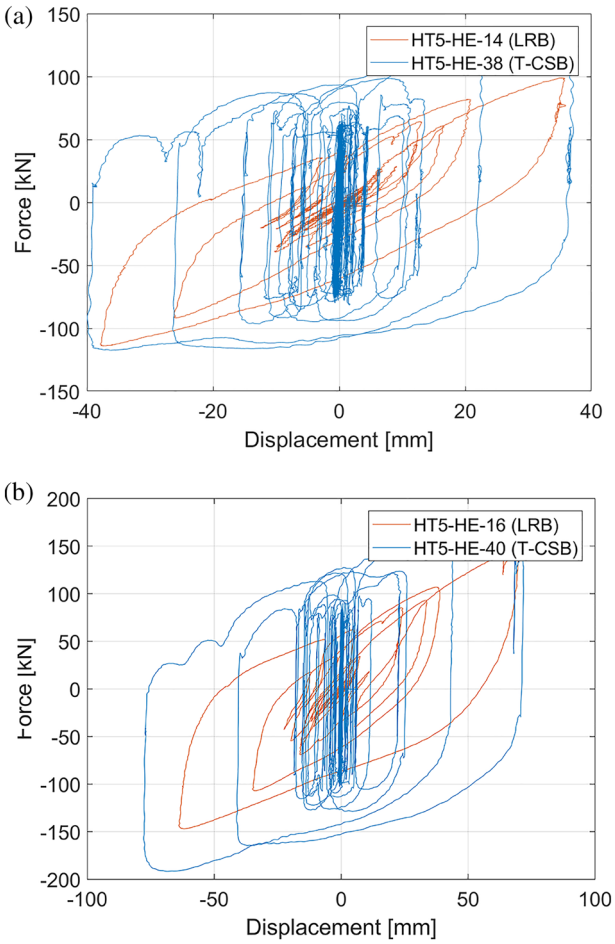

FIGURE 26 Measured hysteretic loops of both seismic isolation devices at (a) peak ground acceleration = 0.35 *g* and (b) peak ground acceleration = 0.50 *g*. LRB, lead rubber bearing; T-CSB, triple curvature concave sliding bearing

simulations, which proved that deck overturning moment was negligible and did not affect the transversal response of the bridge.

3.4 | Experimental results

This section summarizes the main results of the experimental campaign named HT5. In this regard, Table 6 reports the list of experiments and relevant setting. An additional experimental campaign named HT3 and based on pseudodynamic HS was performed, but results are out of the scope of this paper and, therefore, are omitted.

In this regard, Figure 25 compares the displacement history of Pier 2 for all tested isolation devices considering a scaling of the ground motion up to 0.50 *g* of PGA. With regard to the same experiments, Figure 26 compares the measured hysteretic loops of the restoring forces of tested isolation devices.

As reported in Figure 25, the absolute displacement response peak of Pier 2 always remained below 7 mm, regardless of the type of isolation device. Within this range, the real pier would not be damaged. Accordingly, hysteresis loops reported in Figure 26 are characterized by similar displacement and restoring force ranges. These results highlight that investigated isolation schemes exhibit similar performances.

4 | CONCLUSIONS

Most of nonlinear computational frameworks for HS rely on adaptations of existing finite-element software to accommodate the so-called experimental elements, which incorporate a digital interface to a control system, for example, OpenFRESCO or UI-SIMCOR. The finite-element software operates in soft time, for example, on a standard PC, whereas the control system operates in hard real time and manipulates the PS by means of servo-controlled actuators. However, the complexity of finite-element software is not suitable—and not necessary—for hard real-time implementations of fast-time HS, that is, with testing timescale close to one. Moreover, prototype structures emulated via HS can be easily described as lumped parameter systems characterized by a small number of degrees of freedom.

These considerations motivated the development of the computational framework for fast-time HS presented in this paper, which is based on state-space modeling and partitioned time integration. On one hand, precomputed mass and stiffness matrices of substructures plus additional differential equations can be easily used to model nonlinear NSs with hysteretic behavior as state-space systems; on the other hand, partitioned time integration permits coupling of multiple time integration processes with different time step sizes. The time integration of the PS response is performed at the same sampling rate of the real-time control system so as to guarantee continuous actuator trajectories, whereas the NS response can be subsampled compatibly with available computational resources. The resulting simulation code reduces to a time stepping analysis scheme that solves a set of first-order ordinary differential equations and can be easily implemented in MATLAB/SIMULINK. Automatic code generation from such visual programming tools makes the process of developing hard real-time applications straightforward.

Eventually, the HSs of a virtual bridge prototype performed at the Experimental Laboratory of EUCENTRE, Pavia, Italy, demonstrated the effectiveness of the presented computational framework.

ACKNOWLEDGEMENTS

The financial support from the Experimental Laboratory of EUCENTRE, Pavia, Italy, the STRIT project funded by the Italian Ministry of Education, University and Research (MIUR), and the RELUIS-DPC 2014-2018 project funded by the Dipartimento della Protezione Civile, Presidenza del Consiglio dei Ministri, are greatly appreciated. The first author acknowledges the support of the Chair of Structural Dynamics and Earthquake Engineering (Prof. B. Stojadinovic) of ETH Zurich, whereas the third and fourth authors acknowledge funding from the Italian Ministry of Education, University and Research (MIUR) in the frame of the "Departments of Excellence" Grant L. 232/2016 and the SERA Grant Agreement No. 730900.

ORCID

Giuseppe Abbiati https://orcid.org/0000-0002-5048-8505
Oreste S. Bursi https://orcid.org/0000-0003-3072-7414

REFERENCES

1. Pegon P, Pinto A. Pseudo-dynamic testing with substructuring at the ELSA Laboratory. *Earthq Eng Struct Dyn*. 2000;29(7):905-925.
2. Calabrese A, Strano S, Terzo M. Real-time hybrid simulations vs shaking table tests: case study of a fibre-reinforced bearings isolated building under seismic loading. *Struct Control Health Monit*. 2015;22(3):535-556.
3. Bursi OS, Abbiati G, Cazzador E, Pegon P, Molina FJ. Nonlinear heterogeneous dynamic substructuring and partitioned FETI time integration for the development of low-discrepancy simulation models. *Int J Numer Methods Eng*. 2017;112(9):1253-1291.
4. Schellenberg AH, Becker TC. Hybrid shake table testing method: theory, implementation and application to midlevel isolation. *Struct Control Health Monit*. 2016;24(5):e1915.
5. Schellenberg AH, Mahin SA, Fenves GL. "PEER report 2009/104 "Advanced implementation of hybrid simulation"," Pacific Earthquake Engineering Research (PEER) Center, University of California, Berkeley, 2009.
6. Kwon OS, Nakata N, Elnashai A, Spencer B. Technical note a framework for multi-site distributed simulation and application to complex structural systems. *J Earthq Eng*. 2005;9(5):741-753.
7. Pegon P, Magonette G. "Technical report 1.02.167 "Continuous PSD testing with nonlinear substructuring: presentation of a stable parallel inter-field procedure"," European Commission, Joint Research Centre, ELSA, Ispra, Italy, 2002.
8. Bonelli A, Bursi OS, He L, Magonette G, Pegon P. Convergence analysis of a parallel inter-field method for heterogeneous simulations with dynamic substructuring. *Int J Numer Methods Eng*. 2008;75(7):800-825.
9. Bursi OS, He L, Bonelli A, Pegon P. Novel generalized-α methods for inter-field parallel integration of heterogeneous structural dynamic systems. *J Comput Appl Math*. 2010;234(7):2250-2258.
10. Abbiati G, Bursi OS, Caperan P, Di Sarno L, Molina FJ. Hybrid simulation of a multi-span RC viaduct with plain bars and sliding bearings. *Earthq Eng Struct Dyn*. 2015;44(13):2221-2240.
11. Bursi OS, Wang Z, Jia C, Wu B. Monolithic and partitioned time integration methods for real-time heterogeneous simulations. *Comput Mech*. 2012;52(1):99-119.
12. MathWorks, "MATLAB webpage," MathWorks, 7 2 2018. [Online]. Available: https://ch.mathworks.com/. [Accessed 7 2 2018].
13. Makris N, Chang S. Effect of viscous, viscoplastic and friction damping on the response of seismic isolated structures. *Earthq Eng Struct Dyn*. 2000;29(1):85-107.
14. Chang S, Makris N, Whittaker E, Thompson A. Experimental and analytical studies on the performance of hybrid isolation systems. *Earthq Eng Struct Dyn*. 2002;31(2):421-443.
15. Ismail M, Ikhouane F, Rodellar J. The hysteresis Bouc-Wen model, a survey. *Arch Comput Meth Eng*. 2009;16(2):161-188.
16. Mostaghel N. Analytical description of pinching, degrading hysteretic systems. *J Eng Mech*. 1999;125(2):216-224.
17. Brüls O, Arnold M. The generalized-α scheme as a linear multistep integrator: toward a general mechatronic simulator. *J Comput Nonlinear Dyn*. 2008;3(4):41007.
18. Brun M, Batti A, Combescure A, Gravouil A. External coupling software based on macro- and micro-time scales for explicit/implicit multi-time-step co-computations in structural dynamics. *Finite Elem Anal Des*. 2014;86:101-119.
19. Jansen KE, Whiting CH, Hulbert GM. A generalized-α method for integrating the filtered Navier–Stokes equations with a stabilized finite element method. *Comput Methods Appl Mech Eng*. 2000;190(3–4):305-319.
20. Erlicher S, Bonaventura L, Bursi OS. The analysis of the generalized-α method for nonlinear dynamic problems. *Comput Mech*. 2002;28(2):83-104.
21. Patterson MA. An efficient overloaded method for computing derivatives of mathematical functions in MATLAB. *J ACM Trans Math Software (TOMS)*. 2013;17(1):17-36.
22. Peloso S, Pavese A, Casarotti C. Eucentre TREES Lab: Laboratory for Training and Research in Earthquake Engineering and Seismology. In: *Role of Seismic Testing Facilities in Performance-based Earthquake Engineering*. Dordrecht: Springer Netherlands; 2012:65-81.
23. McKenna F. OpenSEES: open system for earthquake engineering simulation. *Comput Sci Eng*. 2011;13(4):58-66.
24. Peloso S, Pavese A. "FRP seismic retrofit for insufficient lap-splice: large scale testing of rectangular hollow section bridge piers," in Proceedings of the ECCOMAS Thematic Conference on Computational Methods in Structural Dynamics and Earthquake Engineering (COMPDYN), Rhodes, Greece, 2009.
25. Iervolino I, Galasso C, Cosenza E. REXEL: computer aided record selection for code-based seismic structural analysis. *Bull Earthq Eng*. 2010;8(2):339-362.
26. Fenz DM, Constantinou MC. Spherical sliding isolation bearings with adaptive behavior: theory. *Earthq Eng Struct Dyn*. 2008;37(2):163-183.
27. Benzoni G, Casarotti C. Effects of vertical load, strain rate and cycling on the response of lead–rubber seismic isolators. *J Earthq Eng*. 2009;13(3):293-312.
28. Wu B, Wang Z, Bursi OS. Actuator dynamics compensation based on upper bound delay for real-time hybrid simulation. *Earthq Eng Struct Dyn*. 2013;42(12):1749-1765.

How to cite this article: Abbiati G, Lanese I, Cazzador E, Bursi OS, Pavese A. A computational framework for fast-time hybrid simulation based on partitioned time integration and state-space modeling. *Struct Control Health Monit*. 2019;e2419. https://doi.org/10.1002/stc.2419